

Lattice-Boltzmann LES modelling of a full-scale, biogas-mixed anaerobic digester

Davide Dapelo^{1*}, Adrian Kummerländer², Mathias J. Krause² and John Bridgeman¹

²Lattice Boltzmann Research Group, Karlsruhe Institute of Technology, Karlsruhe, Germany.

¹School of Engineering, University of Liverpool, Liverpool, United Kingdom.

*Corresponding author(s). E-mail(s): d.dapelo@liverpool.ac.uk;

Abstract

An Euler-Lagrange multicomponent, non-Newtonian Lattice-Boltzmann Method is applied for the first time to model a full-scale gas-mixed anaerobic digester for wastewater treatment. Rheology is modelled through a power-law model and, for the first time in gas-mixed anaerobic digestion modelling, turbulence is modelled through a Smagorinsky Large Eddy Simulation model.

The hydrodynamics of the digester is studied by analysing flow and viscosity patterns, and assessing the degree of mixing through the Uniformity Index method. Results show independence from the grid size and the number of Lagrangian substeps employed for the Lagrangian sub-grid simulation model. Flow patterns are shown to depend mildly on the choice of bubble size, but not the asymptotic degree of mixing.

Numerical runs of the model are compared to previous results in the literature, from a second-ordered Finite-Volume Method approach, and demonstrate an improvement, compared to literature data, of 1,000-fold computational efficiency, massive parallelizability and much finer attainable spatial resolution.

Whilst previous research concluded that the application of LES to full-scale anaerobic digestion mixing is unfeasible because of high computational expense, the increase in computational efficiency demonstrated here, now makes LES a feasible option to industries and consultancies.

29 **Keywords**

30 Lattice-Boltzmann; OpenLB; Anaerobic Digestion, Full-Scale; Non-Newtonian;
31 Euler-Lagrange

32 **Nomenclature**

Δt_{inj}	Time interval between the injection of two bubbles, s
Φ	Phase space
Φ	Sourcing term, kg m^3
Ξ	Collision step, kg m^3
$ \dot{\gamma} $	shear rate magnitude, s^{-1}
$ \dot{\gamma} _{\text{ref}}$	Reference shear rate magnitude, s^{-1}
δ^3, \dots	3D Kroneker delta
δt	Lattice timestep, s
δx	Lattice cell size, m
ϕ	Finite-difference tracer field, m^{-3}
μ	Apparent dynamics viscosity, Pa s
μ_{max}	Apparent dynamics viscosity, maximum range value, Pa s
μ_{min}	Apparent dynamics viscosity, minimum range value, Pa s
μ_{PL}	Apparent dynamic viscosity before turbulence correction, Pa s
ν	Kinematic viscosity, $\text{m}^2 \text{s}^{-1}$
ν_{PL}	Apparent kinematic viscosity before turbulence correction, $\text{m}^2 \text{s}^{-1}$
ν_{ref}	Reference kinematic viscosity, $\text{m}^2 \text{s}^{-1}$
ν_{turb}	Turbulent kinematic viscosity, $\text{m}^2 \text{s}^{-1}$
ρ	Liquid phase density, Kg m^{-3}
σ	Liquid phase shear stress, Pa
τ	Lattice relaxation time, s
\mathbf{A}_K	Acceleration of the K -th Lagrangian sub-grid particle, m s^{-2}
\mathcal{C}	Collision operator, kg m^3
C_d	Drag coefficient
C_{Smago}	Smagorinsky constant
\mathbf{F}_K	Total force acting on the K -th Lagrangian sub-grid particle, N
\mathbf{F}_K^a	Added-mass force acting on the K -th Lagrangian sub-grid particle, N
\mathbf{F}_K^b	Buoyancy force acting on the K -th Lagrangian sub-grid particle, N
\mathbf{F}_K^d	Drag force acting on the K -th Lagrangian sub-grid particle, N
K	Power-law consistency coefficient, Pa s^n
K	(as a subscript) Generic label to a Lagrangian sub-grid particle
M_K	Mass of the K -th Lagrangian sub-grid particle, Kg
Ma	Mach number
\mathcal{P}_K	Tuple representing the K -th Lagrangian sub-grid particle
Re	Reynolds number
Re_p	Particle Reynolds number
R_K	Nominal radius of the K -th Lagrangian sub-grid particle, m
\mathbf{S}	Rate of shear tensor, s^{-1}
\mathcal{S}	Source term operator, kg m^3
\mathbf{U}	Nominal velocity scale, m s^{-1}
UI	Uniformity index
\mathbf{U}_K	Spatial coordinate of the K -th Lagrangian sub-grid particle, m s^{-1}
U_{LB}	Lattice velocity
U_{LB}^0	Reference lattice velocity
\mathbf{X}_K	Spatial coordinate of the K -th Lagrangian sub-grid particle, m

$\mathbf{X}_K^{\text{next}}$	Spatial coordinate of the K -th Lagrangian sub-grid particle, approximated at the nearest lattice node, m
\mathbf{c}	Mesosopic velocity, m s^{-1}
\mathbf{c}_i	i -th discretised lattice (mesoscopic) velocity, m s^{-1}
c_s	Lattice speed velocity, m s^{-1}
d	Bubble diameter, m
f	One-particle density function, kg m^{-3}
$f^{(1)}$	First-order multiscale term of the one-particle distribution function, kg m^{-3}
$f^{(\text{eq})}$	Equilibrium one-particle density function, kg m^{-3}
\mathbf{g}	Acceleration of gravity, m s^{-2}
n	Power-law index
n_x	Number of lattice sites across the tank's diameter
n_x^0	Reference number of lattice sites across the tank's diameter
p	Pressure, Pa
s	Number of Lagrangian subcycles
t	Time, s
\mathbf{u}	Liquid phase velocity, m s^{-1}
u_{surr}	Liquid phase velocity magnitude in the surroundings of a rising biogas bubble, m s^{-1}
w_i	Weight of the i -th component of the equilibrium particle distribution
\mathbf{x}	Discretised lattice spatial coordinate, m
\cdot^*	Dimensionless version of the argument represented by the \cdot
CFD	Computational Fluid Dynamics
CPUs	CPU-second (<i>i.e.</i> , number of seconds a given numerical simulation takes to be run, times number of CPU cores employed)
EU	European Union
FV	Finite-Volume
LB	Lattice-Boltzmann
LES	Large Eddy Simulations
TS	Total solid content
WFD	EU Water Framework Directive
WwTW	Wastewater treatment work

34

1 Introduction

35

36 Over the next decades, the wastewater industry will continue to be subjected to
 37 unprecedented challenges, as worldwide demands for food and clean water are
 38 expected to rise by 50% and 30% respectively [1]. Furthermore, implementation of
 39 the EU Water Framework Directive (WFD) is driving an increase of energy consump-
 40 tion by up to 60% in wastewater treatment works (WwTWs) over the next 10–15
 41 years [2], due to tighter discharge requirements. The wastewater-energy link must be
 42 clearly addressed in order to mitigate, and adapt towards, climate change.

43

44 Since 2009, wastewater treatment works across each major European country
 45 have produced over 1M tonnes sludge per country per year [3]. The preferred
 46 method to treat sludge is mesophilic (22–41 °C) anaerobic digestion with mix-
 ing occurring through biogas injection. Through this process, sludge is degraded by

47 anaerobic bacteria into stable digestate and biogas (a mixture of mainly methane and
48 carbon dioxide). Biogas is usually directed to a combined heat and power unit for
49 energy recovery. Mixing is necessary for correct digestion and can be responsible for
50 anywhere between 17 and 73% of digester energy consumption [4]. This level of con-
51 sumption is largely suboptimal, as experimental evidence [5] shows that input mixing
52 power can be reduced by to 50% without affecting the digestion process. To address
53 mitigation and adaptation to climate change, it is therefore necessary to rethink mix-
54 ing design practices and operation protocols, with the goal of balancing input mixing
55 energy against output biogas production, rather than merely considering digestate
56 quality.

57 Over the years, (segregated) Finite-Volume (FV) Computational Fluid Dynamics
58 (CFD) has been successfully employed to model gas-mixed anaerobic digesters [6–
59 19]. A CFD approach to design and system analysis offers multiple benefits, includ-
60 ing a saving of time and money arising from avoiding lengthy and time-consuming
61 experiments, and providing an insight to flow patterns which are unattainable from
62 optical visualisation techniques (sludge is opaque) or tracer-response methods (which
63 provide no more than a black-box description of the system). This progress has
64 enabled the development of structured modelling protocols to significantly improve
65 energy performance of both new and existing full-scale digester [20]. However,
66 limitations in the industrial applicability of this approach persist, as long simula-
67 tion runtimes (≥ 2 days) render the deployment of the above-mentioned strategies
68 excessively time-consuming. Furthermore, the multi-core parallel run of most com-
69 mon Finite-Volume schemes (*viz.*, up to second-order) is hampered by poor parallel
70 performance [21], mainly due to the high proportion of non-scalable inter-core com-
71 munication operations involved in solving the Poisson pressure equation [22]. Indeed,
72 previous Finite-Volume models of full-scale anaerobic digesters [17, 20, 23] could
73 not scale up beyond 36 cores. As such, traditional Finite-Volume CFD cannot bene-
74 fit from the on-going evolution of high-performance computing. In turn, this makes
75 it impractical, or very time-consuming, to employ accurate but resource-intensive
76 methodologies, *e.g.*, the Large Eddy Simulations (LES). Indeed, no LES model
77 for full-scale gas-mixed anaerobic digestion has been developed so far: only [24]
78 has developed a LES Finite-Volume model for full-scale anaerobic digestion, but
79 for mechanical, not gas, mixing, and concluded that LES is impractical due to the
80 excessive computational expense required.

81 A potential solution to both the problems listed above is offered by the Lattice-
82 Boltzmann (LB) Method, a relatively recent CFD alternative to the Finite-Volume
83 approach with recent industrial applications comprising, among other things, Ball-
84 Grid-Array encapsulation process, heat flux inside refrigerated vehicles, internal-
85 combustion engine and 3D-printed wet-scrubber nozzle [25–28]. Lattice-Boltzmann
86 is essentially a Finite-Difference method equipped with tunable diffusivity [29].
87 Lattice-Boltzmann presents tangible advantages over the traditional Finite-Volume
88 approach, such as: (i) full explicitness free from internal loops, resulting in a well-
89 defined, limited number of floating-point operations per timestep; and (ii) strong
90 parallelizability due to reduced non-scalable inter-core communication thanks to
91 a formal and implementational distinction between non-local and non-linear parts

of the algorithm and non-local access usually limited to first-neighbour cells only. Furthermore, the Lattice-Boltzmann method has the advantage over other models suitable to parallel computing (*viz.*, high-order Finite-Volume, [21]), of (*iii*) implementational simplicity, as its structured grid approach and first-neighbour-only non-local access allow it to avoid complex stencils and to implement boundary conditions in a straightforward manner. Multiphase models, both Euler-Euler [30] and Euler-Lagrange [31–35], are available. A comparison between a Lattice-Boltzmann LES model and its Finite-Volume counterpart applied to a internal-combustion engine [27] showed that the former ran 32 times faster, thus making the usage of LES much more practical: “The faster calculation speed for NWM-LES using LBM is advantageous to address industrial applications and to enable ‘overnight’ calculations that previously took weeks. Therefore, faster design cycles and operating condition tests are feasible”. Coming to anaerobic digestion, a Lattice-Boltzmann model for a laboratory-scale gas-mixed digester [34] has been shown to perform around 180 times faster than its Finite-Volume analogue [14] whilst being able to run on ten times more processors without appreciable efficiency decrease. Thus, Lattice-Boltzmann’s superior numerical efficiency and parallelizability allow much finer grids than Finite-Volume at comparable numerical expense and runtimes, amply compensating for the errors arising from the traditional lack of local mesh refinement, unstructured and body-fitted grids in the traditional Lattice-Boltzmann implementations. It is therefore clear that Lattice-Boltzmann models can deliver a significant benefit to the operation of numerical modelling anaerobic digestion with gas mixing.

The topic of mixing improvement in full-scale anaerobic digestion has been widely investigated through CFD despite severe limitations in validation procedure: the intrinsically opaque and hazardous nature of sludge, as well as the impracticability of taking digesters out of production for experimental purposes, means that no experimental data concerning full-scale anaerobic digesters for wastewater treatment are available in the literature. As a result, there are examples in the literature where researchers provide unvalidated results in full-scale anaerobic digestion [8–10, 13]; rely on full-scale validation conducted on black-box measurements such as impeller power number [36]; or validate a model against flow patterns from a lab-scale setup, and then apply it to the full-scale [14, 17, 20, 23, 37].

Despite the advantages of CFD and, to a greater extent, Lattice-Boltzmann method, for anaerobic digestion modelling, only a limited amount of work has been dedicated to modelling the gas mixing processes [6, 10, 14, 17, 20, 23, 34, 35, 38]; among this, only [34, 35] employed the Lattice-Boltzmann; and finally, none reports full-scale Lattice-Boltzmann models with gas mixing. [34] introduced the first-ever multiphase Lattice-Boltzmann model for gas-mixed anaerobic digestion in a laboratory-scale set-up, and [35] demonstrated that the sub-grid Euler-Lagrange Lattice-Boltzmann method can be successfully employed to model laboratory and full-scale anaerobic digesters. In both [34, 35], the models were validated against laboratory-scale experiments conducted by [14]. However, a knowledge gap persists as no Lattice-Boltzmann model for gas-mixed industrial-scale digesters has been reported in the literature.

136 Within the work reported here, the sub-grid method developed and validated
137 lab-scale in [35] is used for the first time to model a full-scale setup reproducing a
138 real wastewater treatment digester, applying the same approach towards validation
139 of [14, 17, 20, 23, 37] and thereby filling the above-mentioned knowledge gap. Flow
140 and viscosity patterns are analysed, and the degree of mixing is evaluated through
141 the Uniformity Index (UI) method proposed by [9]. The effect of different modelling
142 parameters on the simulation outcome is assessed. The results are discussed and com-
143 pared to previous second-order Finite-Volume work on a similar design [17, 20, 23].
144 It is shown how the Lattice-Boltzmann method offers advantages over the method
145 used therein, and has a clear potential to overcome the issues concerning industrial
146 applicability of CFD-based mixing-improvement strategies described above. Like-
147 wise, it is shown that the introduction of a Lattice-Boltzmann-based model makes the
148 application of LES to full-scale anaerobic digester practically feasible to industries
149 and consultancies.

150 This paper is structured as follows. Sludge is modelled in Section 2: the assump-
151 tions underlying the multiphase model are laid down in Subsection 2.1; then, the
152 model is described within the Lattice-Boltzmann framework in Subsections 2.2
153 and 2.3; finally, the pseudocode algorithm is reported in Subsection 2.4. The model's
154 implementation in OpenLB is reported in Section 3, and a short description of
155 OpenLB and the innovation it has brought in the field of parallel computing is offered
156 in Subsection 3.1. then, the results are reported in Section 4, and specifically: flow
157 patterns (Subsection 4.1); grid independence (Subsection 4.2); mixing efficiency
158 (Subsection 4.3); dependence of the results from the choice of Lagrangian subcycles
159 (Subsection 4.4) and bubble size (Subsection 4.5); and scaling-up (Subsection 4.6).
160 Then, a discussion is performed (Section 5), and conclusions are drawn (Section 6).

161 2 Modelling of sludge

162 Within this work, one of the models described in [35], with the geometry of [17, 23]
163 is used. It is summarised here for the sake of clarity.

164 2.1 Assumptions

165 Sludge is a complex mixture of organic and inorganic solids arranged in fragments
166 of various dimensions (from colloid molecules to sand or gravel), water and biogas
167 bubbles where gas mixing is employed. The range of inter-phase phenomena include
168 bubble-liquid (two-way) and bubble-bubble (four-way) momentum transfer, solid-
169 liquid interactions such as grit sedimentation and scum flotation, and complex liquid
170 rheology characterised by shear thinning, shear banding, yield stress and thixotropy.

171 To simplify the problem of modelling sludge, a sub-grid, two-way coupled
172 Euler-Lagrange model with non-Newtonian rheology and a large-eddy-simulation
173 turbulence model is introduced. The assumptions and simplifications underlying the
174 choice of this model, as well as the justifications underpinning them, are listed as
175 follows.

176 (i) Sedimentation and flotation are ignored because they respectively take place
 177 in years/months and days/weeks, whilst the timescale of the mixing is up to two
 178 hours.

179 (ii) Solid phase is considered as a suspension of liquid phase, and its effect on
 180 the latter is modelled as the liquid phase's non-Newtonian pseudoplastic rheology
 181 [39], with more complex rheological phenomena being ignored. In a pseudoplastic
 182 power-law model, the apparent viscosity μ is a function of the magnitude of the shear
 183 rate $|\dot{\gamma}|$, as follows:

$$\mu = K|\dot{\gamma}|^{n-1}, \quad (1)$$

184 with K and n ($0 < n < 1$) being respectively the consistency and power-law coeffi-
 185 cients. Although both K and n depend on temperature and total solids content [40],
 186 temperature dependence is ignored as K and n are considered constant at the fixed
 187 temperature of 35 °C, this being the ideal temperature for mesophilic conditions.
 188 Table 2 reports typical values of n and K at 35 °C. For the sake of simplicity, sludge
 189 density is set to 1,000 kg m⁻³. Equation 1 returns unphysically high or low appar-
 190 ent viscosity values for low or high values of $|\dot{\gamma}|$ respectively; this is avoided in a
 191 standard way by introducing a minimum and maximum cutoff value for the apparent
 viscosity, μ_{\min} and μ_{\max} .

Table 2: Power-law coefficients, cutoffs and density of sludge at $T=35$ °C. From [40].

TS (%)	K (Pa s ^{n})	n (-)	$ \dot{\gamma} $ range (s ⁻¹)	μ_{\min} (Pa s)	μ_{\max} (Pa s)	Density (kg m ⁻³)
2.5	0.042	0.710	226–702	0.006	0.008	1,000.36
5.4	0.192	0.562	50–702	0.01	0.03	1,000.78
7.5	0.525	0.533	11–399	0.03	0.17	1,001.00
9.1	1.052	0.467	11–156	0.07	0.29	1,001.31
12.1	5.885	0.367	3–149	0.25	2.93	1,001.73

192 (iii) As reported in the following Results sections, the Reynolds number is found
 193 to be comprised between 3,600 and 6,100, and therefore, turbulence is modelled. A
 194 large eddy simulation (LES) model is chosen, and the Smagorinsky constant C_{Smago}
 195 is set to 0.14.

196 (iv) Bubble-bubble interaction, bubble coalescence and breakup are ignored,
 197 as they were found not to occur in experimental work [14]. Conversely, mixing
 198 occurs because of the momentum of the buoyant bubbles being transferred to the
 199 surrounding liquid phase. Therefore, the bubble-liquid interaction must be modelled;
 200 *i.e.* bubble-liquid two-way coupling is considered whereby momentum is transferred
 201 from the liquid phase to the bubbles (“*forward-coupling*”); and from the bubbles to
 202 the liquid phase (“*back-coupling*”).

203 (v) The smallest grid cells used in this work are cubes of 9 cm size, which
 204 are larger than the largest bubble diameter (5 cm). Previous work [35] showed that
 205 liquid phase flow patterns can be effectively reproduced through a sub-grid Euler-
 206 Lagrange model, and consequently, bubbles are considered as pointwise within this
 207 work. Bubbles are also assumed to have the same density of air, *i.e.* 1 kg m⁻³.

2.2 Modelling and simulation: Sub-grid Euler-Lagrange bubbly phase

The dispersed bubbly phase is modelled as a collection of sub-grid elements \mathcal{P}_K , or “particles” [34, 41] — one (spherical) bubble per particle. As rotational effects and deviations from sphericity were found to be negligible in previous work [14, 34], it is possible to represent each \mathcal{P}_K as a tuple of numbers consisting of: coordinate \mathbf{X}_K , velocity \mathbf{U}_K , acceleration \mathbf{A}_K , nominal radius R_K and mass M_K :

$$\mathcal{P}_K \equiv (\mathbf{X}_K, \mathbf{U}_K, \mathbf{A}_K, R_K, M_K) . \quad (2)$$

At any Lattice-Boltzmann update, each \mathcal{P}_K within the domain is updated separately via verlet integration of Newton’s second law [42] over a number s of “Lagrangian subcycles” with Lagrangian timestep $\delta t/s$:

$$\mathbf{F}_K = M_K \mathbf{A}_K . \quad (3)$$

The resultant \mathbf{F}_K of the forces acting on \mathcal{P}_K is modelled as a sum of buoyancy \mathbf{F}_K^b , added mass \mathbf{F}_K^a and gravity \mathbf{F}_K^d :

$$\mathbf{F}_K = \mathbf{F}_K^b + \mathbf{F}_K^a + \mathbf{F}_K^d . \quad (4)$$

Forward-coupling is achieved by modelling \mathbf{F}_K^b , \mathbf{F}_K^a and \mathbf{F}_K^d in terms of the liquid phase’s local values of the macroscopic fields: in [35], different models were tested, and the best results in terms of both convergence and numerical expense were achieved when the values of the liquid phase density and velocity fields ρ and \mathbf{u} at the K -th particle’s position \mathbf{X}_K were determined through linear interpolation across the cells surrounding \mathcal{P}_K ; conversely, the value of the kinematic viscosity ν was approximated to the nearest cell $\mathbf{X}_K^{\text{next}}$. The same approach is then adopted here. For buoyancy we have:

$$\mathbf{F}_K^b = - \left[\frac{4}{3} \pi R_K^3 \rho(\mathbf{X}_K) - M_K \right] \mathbf{g} \quad (5)$$

with \mathbf{g} being the acceleration of gravity. Added mass is given by:

$$\mathbf{F}_K^a = - \frac{1}{2} \rho(\mathbf{X}_K) \frac{4}{3} \pi R_K^3 \frac{d}{dt} [\mathbf{U}_K - \mathbf{u}(\mathbf{X}_K)] \simeq - \frac{1}{2} \rho(\mathbf{X}_K) \frac{\pi}{6} d_K^3 A_K . \quad (6)$$

The drag force is defined as:

$$\mathbf{F}_K^d = - \frac{1}{2} \rho(\mathbf{X}_K) C_d (\text{Re}_p) \pi R_K^2 |\mathbf{U}_K - \mathbf{u}(\mathbf{X}_K)| [\mathbf{U}_K - \mathbf{u}(\mathbf{X}_K)] . \quad (7)$$

As in [35], Morsi’s drag coefficient [43] C_d is used. The particle Reynolds number Re_p is evaluated as:

$$\text{Re}_p = \frac{2R_K |\mathbf{U}_K - \mathbf{u}(\mathbf{X}_K)|}{\nu(\mathbf{X}_K^{\text{next}})} . \quad (8)$$

2.3 Modelling and simulation: Lattice-Boltzmann Method for the fluid phase

The Lattice-Boltzmann model solves the one-particle density function $f(\mathbf{x}, \mathbf{c}, t)$, which is defined as the probability of finding one ideally pointwise and indivisible portion of fluid with velocity in $[\mathbf{c}, \mathbf{c} + d\mathbf{c}]$ and position in $[\mathbf{x}, \mathbf{x} + d\mathbf{x}]$ at the time t . The method is mesoscopic insofar as the observable macroscopic fields of density $\rho(\mathbf{x}, t)$, velocity $\mathbf{u}(\mathbf{x}, t)$ and shear stress $\sigma(\mathbf{x}, t)$ are not directly resolved—rather, they are evaluated from f 's first three moments [44]:

$$\rho = \int f d\mathbf{c}; \quad (9)$$

$$\rho \mathbf{u} = \int f \mathbf{c} d\mathbf{c}; \quad (10)$$

$$\rho \mathbf{u} \otimes \mathbf{u} = \sigma + \int f \mathbf{c} \otimes \mathbf{c} d\mathbf{c}. \quad (11)$$

f 's continuity equation in the phase space $\Phi(\mathbf{x}, \mathbf{c})$ takes the name of the Boltzmann equation:

$$(\partial_t + \mathbf{c} \cdot \nabla) f = \mathcal{C}[f]. \quad (12)$$

The “collision operator” \mathcal{C} is a source-sink term, modelling the effect of f of inter-particle collisions taking place within the cube $[\mathbf{x}, \mathbf{x} + d\mathbf{x}]$ between t and $t + dt$. Under the diluted gas assumption (which is considered to hold in the work presented here), only binary collisions are accounted for in \mathcal{C} . Under the widely-adopted Bhatnagar-Gross-Krook (BGK) hypothesis [45], collisions occur isotropically and induce a relaxation of f towards an equilibrium distribution $f^{(\text{eq})}$ with relaxation time τ :

$$\mathcal{C}[f] = -\frac{f - f^{(\text{eq})}}{\tau}. \quad (13)$$

The equilibrium distribution is the Maxwell equilibrium distribution [44]:

$$f^{(\text{eq})}(\mathbf{x}, t) := \rho(\mathbf{x}, t) \left(\frac{1}{2\pi c_s^2} \right)^{3/2} \exp \left\{ -\frac{[\mathbf{u}(\mathbf{x}, t)]^2}{2c_s^2} \right\}, \quad (14)$$

where velocity and density are evaluated through Equations 9 and 10, and c_s is the speed of sound.

Simulations consist of trajectories on the discretized phase space, with constant timestep δt . The phase space $\Phi(\mathbf{x}, \mathbf{c})$ is discretized as follows. The (spatial) discretized computational domain is defined as a 3D cubic lattice, with δx being the distance between two first-neighbouring sites. The discretized velocity space is generated by a set of vectors $\{\mathbf{c}_0, \dots, \mathbf{c}_{q-1}\}$ not mutually independent. \mathbf{c}_0 is the zero vector; the others point from one lattice site to its first neighbour and have module $\delta x/\delta t$; or to its second neighbour and have module $\sqrt{2} \delta x/\delta t$; or to its third (module $\sqrt{3} \delta x/\delta t$). The different choices of discretization are conventionally labelled through a tag *DdQq*: d represents the spatial dimension (in this work, 3); q

264 the number of vectors spanning the velocity space. In place of $f(\mathbf{x}, \mathbf{c}, t)$ we now
 265 have the discretized set $f_i(\mathbf{x}, t)$, where the latter is defined as the probability of find-
 266 ing one portion of fluid at the lattice site \mathbf{x} with velocity \mathbf{c}_i at the time t . The zeroth,
 267 first and second moments of f (Equations 9, 10 and 11) are evaluated as summations,
 268 in place of integrals, over the velocity set:

$$\rho = \sum_i f_i ; \quad (15)$$

269

$$\rho \mathbf{u} = \sum_i f_i \mathbf{c}_i ; \quad (16)$$

270

$$\rho \mathbf{u} \otimes \mathbf{u} = \sigma + \sum_i f_i \mathbf{c}_i \otimes \mathbf{c}_i . \quad (17)$$

271 Using a discretized velocity space induces a discretization error—however, this error
 272 source can be removed if the Maxwell equilibrium function (Equation 14) is written
 273 as a linear combination of Hermite polynomials. To ensure density and momentum
 274 conservation, only the Hermite polynomials up to the second order are needed [44].
 275 As such, the discretized equilibrium function reads as:

$$f_i^{(\text{eq})} = w_i \rho \left[1 + \frac{\mathbf{u} \cdot \mathbf{c}_i}{c_s^2} + \frac{(\mathbf{u} \cdot \mathbf{c}_i)^2 - c_s^2 u^2}{2c_s^4} \right] . \quad (18)$$

276 The values of the weights are set in a standard way depending of the specific DdQp
 277 lattice. Similarly, the speed of sound is defined as:

$$c_s := \frac{1}{\sqrt{3}} \frac{\delta x}{\delta t} . \quad (19)$$

278 The application of Equations 9 and 10 [44] allows evaluation of the macroscopic
 279 fields and recovery of the adiabatic dynamics with a Mach-number-dependant com-
 280 pressibility error of Ma^2 . If the BGK assumption (Equation 13) is adopted the
 281 Boltzmann Equation 12 is discretized into the Lattice-Boltzmann Equation:

$$f_i(\mathbf{x} + \mathbf{c}_i \delta t, t + \delta t) = f_i(\mathbf{x}, t) - \frac{f_i(\mathbf{x}, t) - f_i^{(\text{eq})}(\mathbf{x}, t)}{\tau} . \quad (20)$$

282 Implementation of Equation 20 is split into two steps: a local, non-linear *collision*:

$$\Xi_i(\mathbf{x}, t) = f_i(\mathbf{x}, t) - \frac{f_i(\mathbf{x}, t) - f_i^{(\text{eq})}(\mathbf{x}, t)}{\tau} ; \quad (21)$$

283 and a linear, non-local *streaming*:

$$f_i(\mathbf{x} + \mathbf{c}_i, t + \delta t) = \Xi_i(\mathbf{x}, t) . \quad (22)$$

284 A multiscale (“Chapman-Enskog”) expansion shows that the Lattice-Boltzmann
 285 Equation 20 reproduces the incompressible Navier-Stokes equations under the limit
 286 $\text{Ma} \ll 1$ [44]. Pressure and kinematic viscosity take the values:

$$p := \rho c_s^2, \quad \nu := c_s^2 \left(\tau - \frac{\delta t}{2} \right). \quad (23)$$

287 Non-Newtonian rheology and turbulence are accounted for following [34, 35].
 288 The relaxation time is treated as a field $\tau(\mathbf{x}, t)$ rather than a parameter; its value is
 289 stored alongside $f_i(\mathbf{x}, t)$ and initialised at the first timestep by inverting the second
 290 of Equations 23 using a bespoke reference value ν_{ref} for the kinematic viscosity (see
 291 Section 3). τ is then updated locally at every timestep before the collision phase
 292 (Equation 21), as follows:

293 1. Power-law rheology is modelled as in [46]. The rate of shear tensor $S_{\alpha\beta} \equiv$
 294 $\frac{1}{2}(\partial_\alpha u_\beta + \partial_\beta u_\alpha)$ is evaluated locally from the second momentum of the
 295 first-order multiscale term of f , defined as $f_i^{(1)}$ [44]:

$$\begin{aligned} \mathbf{S}(\mathbf{x}, t) &= -\frac{1}{2\rho c_s^2 \tau(\mathbf{x}, t)} \sum_i f_i^{(1)}(\mathbf{x}, t) \mathbf{c}_i \otimes \mathbf{c}_i \\ &\simeq -\frac{1}{2\rho c_s^2 \tau(\mathbf{x}, t)} \sum_i \left[f_i(\mathbf{x}, t) - f_i^{(\text{eq})}(\mathbf{x}, t) \right] \mathbf{c}_i \otimes \mathbf{c}_i. \end{aligned} \quad (24)$$

296 Dynamic viscosity $\mu_{\text{PL}}(\mathbf{x}, t)$ and, consequently, kinematic viscosity $\nu_{\text{PL}} \equiv$
 297 μ_{PL}/ρ are obtained from the power-law equation 1 through the substitution:

$$|\dot{\gamma}| \equiv \sqrt{2 \mathbf{S} : \mathbf{S}}, \quad (25)$$

298 and then τ is recalculated from the second of Equations 23, with ν_{PL} being used
 299 instead of ν .

300 2. Smagorinsky turbulence is modelled as in [47]. The shear rate magnitude $|\dot{\gamma}|$ is
 301 calculated after power-law correction by reapplying Equations 24 and 25. The
 302 Smagorinsky closure with $C_{\text{Smago}} = 0.14$ is then applied in order to compute
 303 the turbulent linematic viscosity:

$$\nu_{\text{turb}} = \nu_{\text{PL}} + C_{\text{Smago}} |\dot{\gamma}|. \quad (26)$$

304 The final value of τ is then calculated by inverting once more the second of
 305 Equations 23, with ν_{turb} in place of ν .

306 The momentum transfer from bubbles to liquid phase (*viz.*, back-coupling) can
 307 be included by modifying the Lattice-Boltzmann Equation 20 through a general pro-
 308 cedure, due to [48]: a momentum source term due to a body force is added to the

309 Lattice-Boltzmann Equation 20:

$$f_i(\mathbf{x} + \mathbf{c}_i, t + \delta t) = f_i(\mathbf{x}, t) - \frac{f_i(\mathbf{x}, t) - f_i^{(\text{eq})}(\mathbf{x}, t)}{\tau} + \left(1 - \frac{1}{2\tau}\right) \mathcal{S}_i(\mathbf{x}, t) \quad (27)$$

310 and consequently, the collision Equation 21:

$$\Xi_i(\mathbf{x}, t) = f_i(\mathbf{x}, t) - \frac{f_i(\mathbf{x}, t) - f_i^{(\text{eq})}(\mathbf{x}, t)}{\tau} + \left(1 - \frac{1}{2\tau}\right) \mathcal{S}_i(\mathbf{x}, t), \quad (28)$$

311 where the source term \mathcal{S}_i is a function of a particle-dependent forcing term Φ :

$$\mathcal{S}_i := w_i \left[\frac{\mathbf{c}_i - \mathbf{u}}{c_s^2} + \frac{(\mathbf{c}_i \cdot \mathbf{u}) \mathbf{c}_i}{c_s^4} \right] \cdot \Phi. \quad (29)$$

312 For the specific case of implementing the back-coupling, [35] proposed different
313 models. The best performing in terms of convergence and numerical expense con-
314 sisted of equating the forcing Φ (in Equation 29) to $-\mathbf{F}_K$ (in Equation 4) to the most
315 near cell from \mathcal{P}_K , and summing over the particles and the number of Lagrangian
316 subcycles occurring within a Lattice-Boltzmann update:

$$\Phi = - \sum_s \sum_K \mathbf{F}_K \delta_{\mathbf{x}, \mathbf{X}_{\text{next}}}^3. \quad (30)$$

317 Finally, Equation 16 is modified as follows:

$$\rho \mathbf{u} = \sum_i f_i \mathbf{c}_i + \frac{1}{2} \sum_i \mathcal{S}_i \mathbf{c}_i. \quad (31)$$

318 2.4 Simulation algorithm

319 The model follows Algorithm 1 below.

320 3 Numerical experiments: Setup

321 A cylindrical digester with an inclined base as [17, 23] is simulated (Fig. 1). A series
322 of twelve nozzles, placed at equal distances along a circular manifold above the
323 sloped bottom of the tank, is considered. Table 3 reports the geometric details. Mix-
324 ing occurs through a circular manifold of 12 rectangular leaf-sparger nozzles with an
325 equivalent diameter d_{noz} . A set of material numbers is defined to facilitate boundary
326 condition treatment — in other words, a n integer is assigned to a given portion of
327 computational domain. Following Figures 1b and 1c, material number 0 is assigned
328 to out-of-domain cells which do not undertake any lattice operation; 1 to the bulk
329 and is subjected to lattice update but not to boundary conditions; 2 to the wall and
330 floor boundaries and is subjected to both lattice update and bespoke boundary condi-
331 tions; 3 to the liquid phase's free surface and is subjected only to bespoke boundary
332 conditions.

Algorithm 1 General algorithm

Initialize Lattice-Boltzmann ($\Phi = \mathbf{0}$; ρ , \mathbf{u} , τ)
for *timestep*: $t = 0$ to t_{\max} by δt **do**
 Update τ : Equations 23, 24, 25, 1 and 26
 Collide: Equation 28
 Streaming: Equation 22
 Apply boundary conditions
 Create particles depending on value of t **Reset** Φ
 for *Particle* \mathcal{P}_K : $K = 1$ to K_{\max} by 1 **do**
 Remove \mathcal{P}_K if exits the computational domain
 for *Lagrangian subcycle*: $s = 1$ to s_{\max} by 1 **do**
 Verlet integration: Equation 3
 Increase Φ as follows:

$$\Phi \ += \ -F_K \delta_{\mathbf{x}, \mathbf{x}^{\text{next}}}^3 \quad (32)$$

end for
 end for
end for

333 The Reynolds number Re is evaluated as:

$$Re = \frac{U d_{\text{noz}}}{\nu_{\text{ref}}} . \quad (33)$$

334 The reference velocity U is the theoretical asymptotic rising bubble velocity, obtained
335 by imposing a static balance between buoyancy and drag force using Morsi's model
336 [43], multiplied by a heuristic correction set to 0.25 [35]. The reference kinematic
337 viscosity ν_{ref} is evaluated through substitution of the reference shear rate $|\dot{\gamma}|_{\text{ref}}$ onto
338 the rheology characteristic equation 1, with the former being defined as the shear rate

Table 3: Details of the digester geometry, from [17, 23]. Sludge feed inlet is located on a side wall, at a height $h/4$ below the top sludge level. Courtesy of Severn Trent Water Ltd.

External diameter	D_{ext}	14.63 m
Diameter at the bottom of the frustum	D_{int}	1.09 m
Cylinder height	h	14 m
Frustum height	h_0	3.94 m
Distance of original nozzle series from axis	R_1	1.83 m
Distance of new nozzle series from axis	R_2	5.49 m
Distance of nozzles from bottom	h_{noz}	0.3 m
Leaf sparger's equivalent diameter	d_{noz}	9.35 cm
Gas flow rate per nozzle	q_{noz}	$2.3585 \cdot 10^{-3} \text{ m}^3 \text{ s}^{-1}$

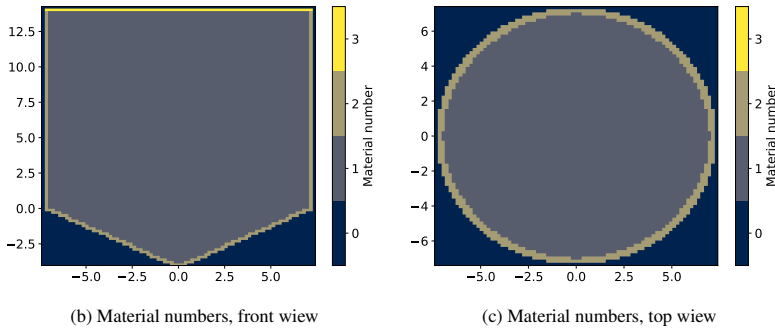
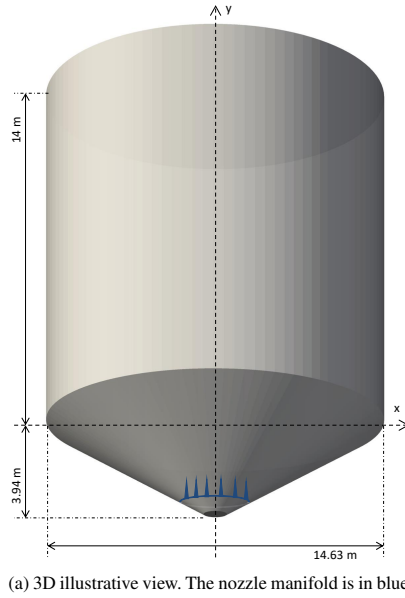


Fig. 1: Computational domain

339 occurring around an asymptotically rising bubble:

$$|\dot{\gamma}|_{\text{ref}} = \frac{U - u_{\text{surr}}}{2d} \simeq \frac{U}{2d} \quad (34)$$

340 because the velocity of the portion of liquid phase surrounding a rising bubble u_{surr}
 341 is negligible if compared to the asymptotic rising bubble velocity U . Re was found to
 342 span between 3,600 (15 mm bubble diameter) and 6,100 (50 mm bubble diameter).

343 The simulations are performed on D3Q27 cubic lattices with linear dimension
 344 n_x spanning from 30 to 160 lattice sites across the diameter D_{ext} , respectively
 345 corresponding to total numbers of cells spanning from 27,344 to 4,271,774. The

dimensionless velocity $U_{\text{LB}} \equiv \delta x / \delta t \cdot 1 \text{ s/m}$ is set according to diffusive scaling:

$$U_{\text{LB}} = U_{\text{LB}}^0 \frac{n_x^0}{n_x}, \quad (35)$$

with $U_{\text{LB}}^0 = 0.15$ and $n_x^0 = 60$. Simulated time spans between 600 and 3,600 s. Free-slip boundary condition is defined for the top free surface (material number 2), and Bouzidi no-slip for walls and bottom (material number 1). The maximum values of y^+ around the walls are found to be 30, 13 and 5 for 2.5%, 5.4% and 7.5% TS respectively, and the average value were respectively 4, 0.16 and 0.08; as such, no wall function is implemented. At the initial timestep, the fluid phase is quiescent and no bubbles are present in the system. Bubbles of diameter $15 < d < 50$ mm are introduced in the computational domain (*viz.*, a new tuple \mathcal{P}_K is defined) one at a time, at a position h_{noz} above the sloping base of the tank. The time interval between two bubble injection is defined as follows:

$$\Delta t_{\text{inj}} = \frac{\pi d^3}{6 q_{\text{noz}}}. \quad (36)$$

As Δt_{inj} is in general not a multiple of δt , bubbles are in practice injected at the first subsequent timestep. The bubbles crossing the liquid surface are deleted.

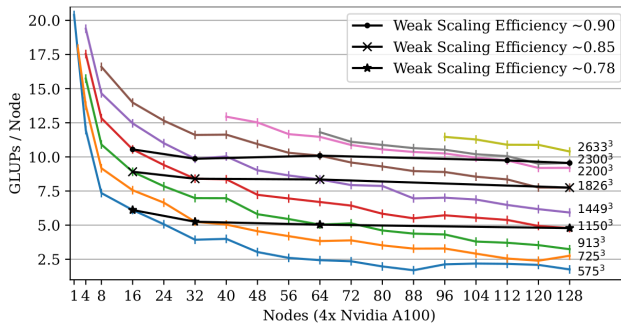
3.1 OpenLB and Lattice-Boltzmann for platform-transparent saturation of modern HPC machines

The Lattice-Boltzmann is particularly suitable for extreme- and exa-scale simulations of fluid flows [49, 50] as, contrarily to conventional numerical techniques, close-to-optimal speedups are reachable. For example, LES of fluid flows in an injector with Lattice-Boltzmann-implemented in OpenLB (www.openlb.net) allow a speedup of 32 (simulation) and 424 (meshing) compared to Finite-Volume implementations in OpenFOAM (www.openfoam.org) on a similar setup with fixed accuracy [27].

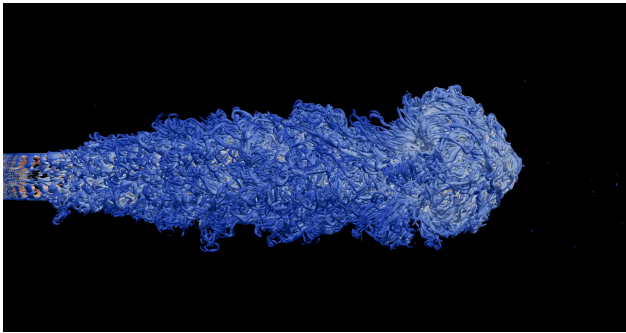
The open-source C++ Lattice-Boltzmann framework OpenLB (<https://www.openlb.net/>) has been continuously developed since 2006. Krause (IAN-M/MVM/KIT). OpenLB contains a broad range of LBM implementations for several classes of partial differential equations (PDEs) for transport multi-physics including initial, boundary, and coupling methods [51]. Besides highly efficient simulations of turbulent, reactive, particulate and thermal fluid flow models, even coupled radiative transport or melting and conjugate heat transfer are realizable [27, 52–55].

Specifically designed for large scale data generation, OpenLB supports efficient and platform-transparent executions, both on single-instruction-multiple-data (SIMD, vectorization) central processing units (CPUs), and general-purpose graphical processing units (GPGPUs) [56]. This is augmented by virtual memory manipulation and automatic code generation in order to reduce the arithmetic load per kernel [57], saturating the available memory bandwidth on current CPU and GPU targets [58]. The parallel efficiency of OpenLB was recently evaluated at up to perfect 1.0 (weak scaling) and very good 0.94 (strong scaling) on the HoreKa supercomputer

382 (https://www.scc.kit.edu/dienste/horeka.php, 66/Top500 June 2022) at SCC (KIT),
 383 using both CPU-only and accelerated GPU partitions (Fig. 2). At the moment, a peak



(a) Scalability of OpenLB 1.5 on HoreKa (multi-GPU execution MPI & CUDA) up to the max. number of nodes allocatable [58]. Throughput in giga (10^9) lattice (cells) updates per second (GLUPs) on the y -axis, for resolutions (N per coordinate axis) labeled on the right.



(b) Q -Criterion iso-contours of GPU-based 3D turbulent nozzle flow simulation using 2.5 billion cells [58]. Colours indicate velocity magnitude from low (blue) to high (orange).

Fig. 2: OpenLB scaling-up on HoreKa

383

384 amount of 1.3×10^{12} grid cell updates per second is realizable on 128 accelerator

385 nodes with 4x NVIDIA A100 GPUs each.

4 Numerical experiments: Results

The simulations are run on one 40-core Lenovo ThinkSystem SR65 CPU. The computational expense spans between 500 and 45,000 CPUs (cumulative figure summed across the cores), depending on the run. OpenLB (www.openlb.net) version 1.3 [51, 59], a generalistic open-source library for parallel Lattice-Boltzmann modelling, equipped with optimized load-balancing strategies [60] and a vectorised A-A streaming algorithm [61], is used.

4.1 Flow patterns

Figure 3 shows snapshots of flow patterns at different times ($t = 300$ and 600 s) for different values of TS. The numbers around the plots and in all the following refer to the spatial coordinates as Figure 1a. Qualitatively, high-velocity narrow areas, with velocity directed vertically upwards, are observed above the nozzle locations; this corresponds to the drag effect exerted by rapidly-rising bubbles to the liquid phase. As the rapidly-rising flow approaches the liquid surface, it is deviated in a radial direction and then, as it approaches the walls, downwards. The flow is finally directed towards the rising columns, forming a toroidal vortex. Smaller-scale structures are also present, indicating the turbulent nature of the flow. The snapshots display fluctuations over time around this general description; this is in agreement with the fact that turbulence is modelled through LES. The large-scale flow patterns remain practically unchanged irrespective of the value of TS: the only qualitative aspect that varies depending of the value of TS is the relative prominence of the small-scale structures connected to turbulence; such structures tend to smooth out as the TS increases. This is in agreement with the fact that Re decreases (and therefore, the flow is less turbulent) as TS increases.

A quantitative description is offered by the coordinates of the vortex. For every timestep, the vortex is found by searching the x - y position minimizing the velocity magnitude within the square window $[3.0 \text{ m}, 6.5 \text{ m}] \times [9.5 \text{ m}, 13.0 \text{ m}]$ starting from an initial guess of $(5.0 \text{ m}, 11.0 \text{ m})$. The resulting vortex position is marked with a red cross in the snapshot of Figure 3, and tracked over time in Figure 4. As in the case of the flow patterns, the vortex position oscillates around an average value, as expected from a LES model. For all the TS values, the stationary-oscillating regime is reached after an initial transient period of around ~ 200 s. Both the average and the statistical standard error (the latter being computed on the same number of samples for all the runs) have similar values for all the values of TS, thereby confirming the qualitative observation of unchanging large-scale flow patterns irrespective of the value of TS.

In Figure 5, snapshots of the apparent viscosity are reported. The viscosity patterns become more evident and less uniform as TS rises, indicating a more prominent power-law behaviour for higher values of TS.

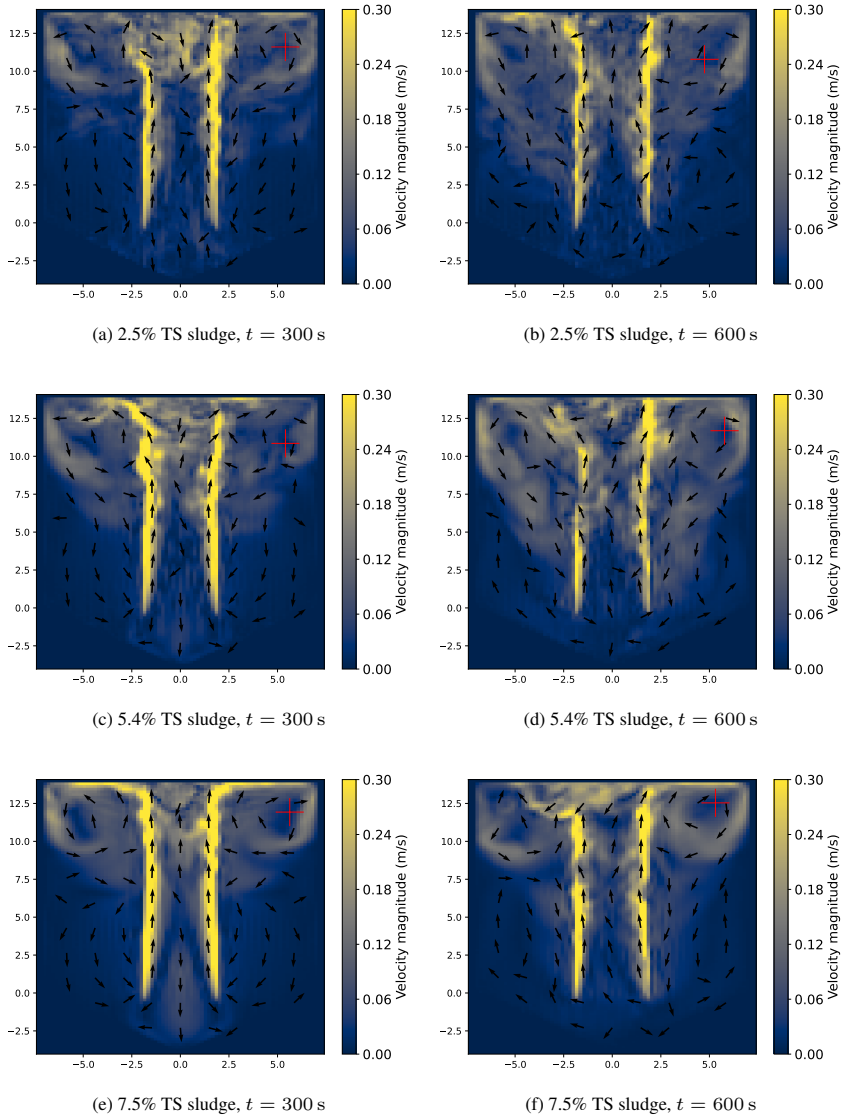


Fig. 3: Flow patterns and vortex position, $n_x = 80$, 50 mm bubble size.

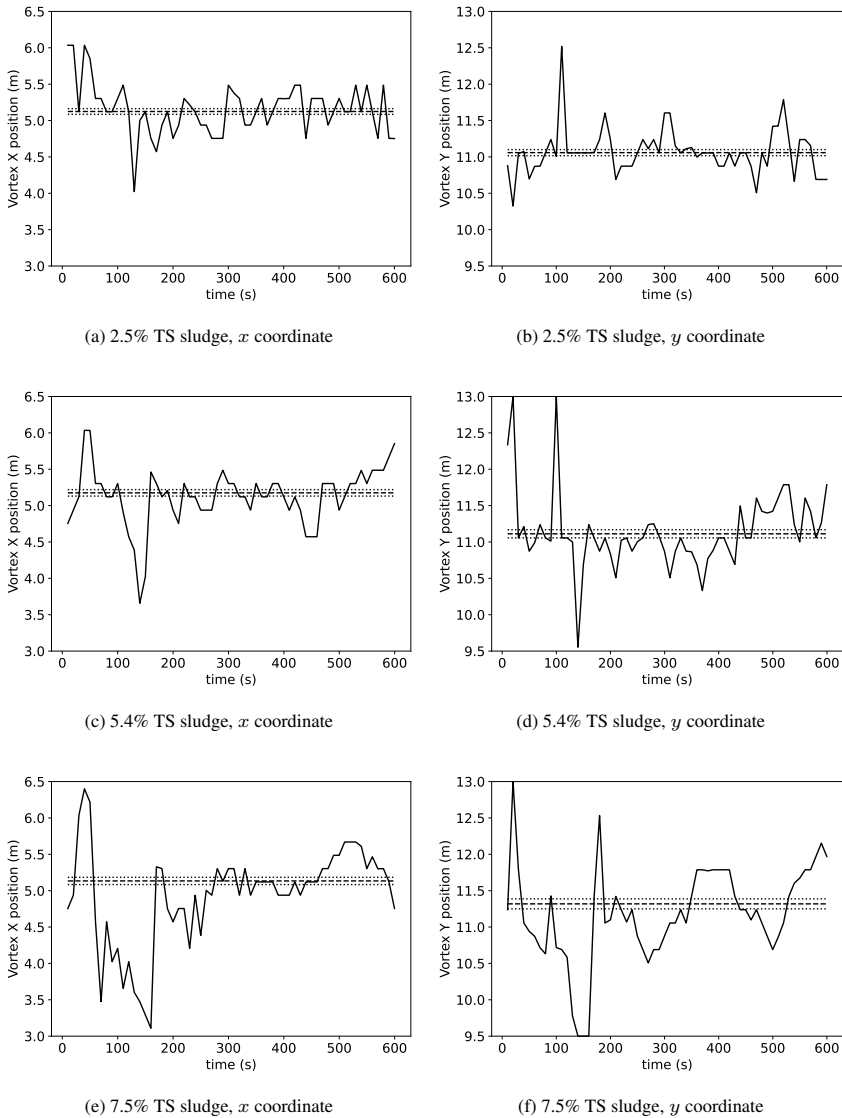


Fig. 4: Vortex coordinates over time, $n_x = 80$, 50 mm bubble size. Solid lines: instantaneous values. Dashed lines: averages, computed from 200 s onwards. Dotted lines: statistical standard errors computed from adapted standard deviations, computed from 200 s onwards.

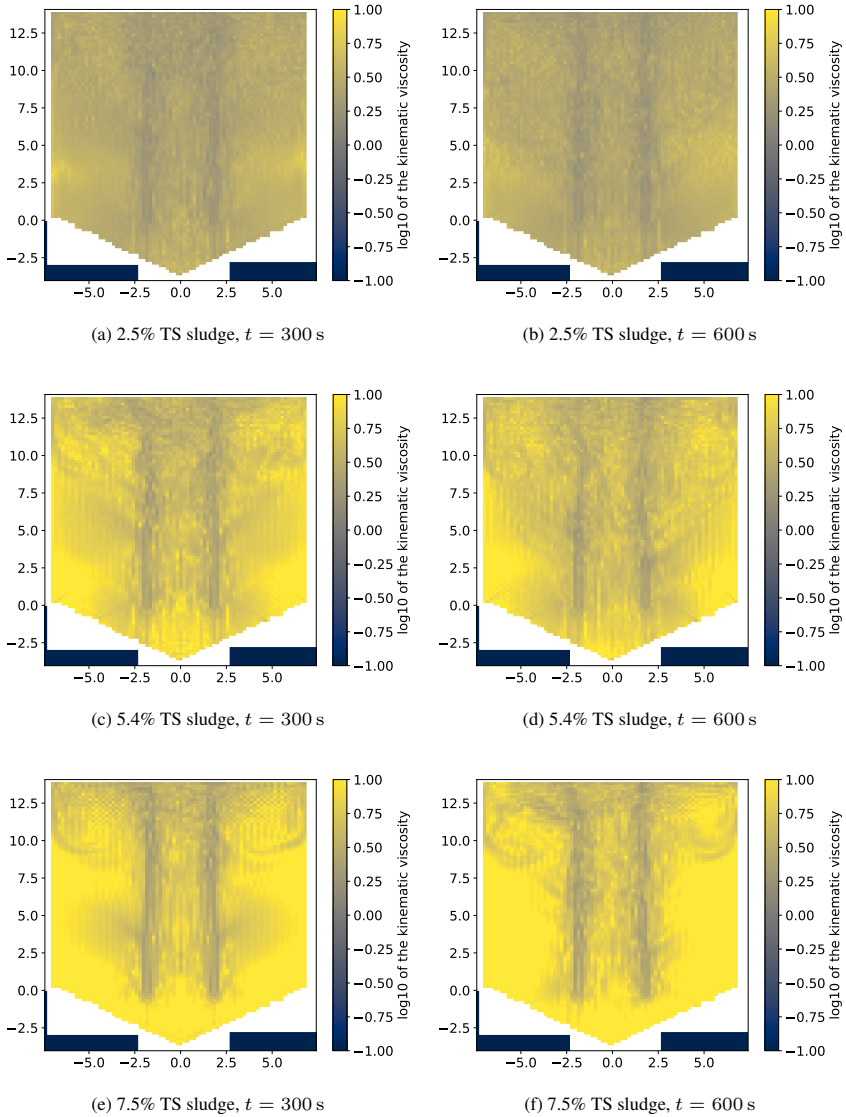


Fig. 5: Apparent viscosity over characteristic viscosity, $n_x = 80$, 50 mm bubble size.

424 **4.2 Grid independence**

The grid independence test is reported in Figure 6. The test is performed over the

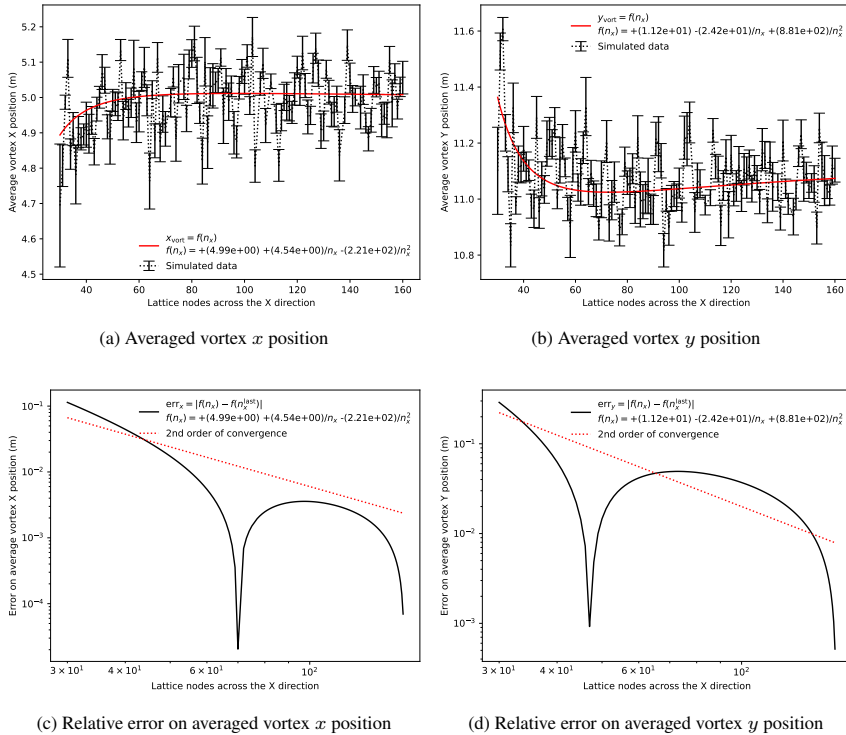


Fig. 6: Averaged vortex position and relative error, 2.5% TS sludge, 50 mm bubble size. Average performed for $t \geq 200$ s.

425
 426 vortex coordinate, with the average being taken for each run by averaging between
 427 the instantaneous values for $200 \text{ s} \leq t \leq 600 \text{ s}$ and errorbars as in Figure 4. The
 428 curves display rapid oscillations. Despite this, a best fit against a function of the type
 429 $f(n_x) = a + b/n_x + c/n_x^2$ shows that the values oscillate around an approximately
 430 horizontal asymptote for $n_x \gtrsim 80$, with a relative error (defined as the absolute value
 431 of the relative difference between the datum and the series' last value) comprised
 432 between 0.2 and 2%. It is therefore possible to consider the results as grid independ-
 433 ent for $n_x > 80$, and the value of $n_x = 80$ is chosen for all the other runs reported in
 434 this work as the best compromise between accuracy and numerical expense.

4.3 Uniformity Index

In [20, 23], the uniformity index (UI), as introduced in [9], was found to be the best single-number quantitative criterion to assess mixing. Given a numerical macroscopic scalar field (“tracer”) ϕ evolving according to an advection-diffusion equation with zero diffusivity:

$$\partial_t \phi + (\mathbf{u} \cdot \nabla) \phi = 0, \quad (37)$$

the uniformity index is defined in a cubic lattice as:

$$\text{UI} := \frac{1}{2 \langle \phi \rangle} \langle |\phi - \langle \phi \rangle| \rangle, \quad (38)$$

with $\langle \cdot \rangle$ being the average over the lattice sites. As a consequence of how it is defined, the value of UI varies between 0 for perfect mixing to 1 for complete inhomogeneity. The tracer ϕ is solved through an explicit Finite-Volume method as in [62]. The first-order upwind scheme for the advection term is preferred over the central second-order for the sake of numerical stability. No negative-diffusivity correction is set [62].

Figure 7 shows the evolution of the tracer ϕ over time up to $t = 600$ s, when ϕ being initialised to 0 almost everywhere, and to 1 in single cells evenly distributed throughout the computational domain (Figure 7a). This initial condition is labelled as “Sparse”. After 10 s from the start of the simulation (Figure 7b), the positions of the pockets with non-zero ϕ remain unaltered, showing that the flow patterns have not yet developed enough to displace them away from their original positions. However, numerical diffusion is evident, and no improvement is observed when negative anti-diffusion is set — this is the reason why anti-diffusion is not set in the work reported here. As a result, despite the evolution towards homogenisation (Figures 7c and 7d) and decrease of the uniformity index (Figure 7e), the latter displays an evident grid dependence with its value at given timesteps depends on grid size (Figure 7f), as numerical diffusion depends on δx [62].

In Figure 8, another initial condition for the scalar tracer ϕ is proposed, under the name of “Ball”. ϕ is initialised to 0 everywhere and to 1 in a sphere sideways (Figure 8a), around the location of the inlet [17, 23]. At the start of the run, the bulk of non-zero concentration field appears to be advected downwards by the flow patterns with marginal diffusion phenomena (Figure 8b), until the tracer finally starts to be spread across the computational domain, after being brought in contact with the rising bubble column (Figures 8c and 8d). Only at that point does the uniformity index start to fall significantly (Figure 8e). This description is in agreement with [23], where new sludge just injected into the system finds itself in a position analogous to the scalar tracer described here and in the cited article, and initially undertakes only a poor level of mixing.

The observation of negligible diffusion phenomena (Figure 8b) is corroborated by the analysis of the behaviour of the uniformity index for different values of n_x (Figure 8f) fitted against a function of the type $\sum_n n_x^{-n}$, $0 \leq n \leq 4$, and the corresponding relative error (Figure 8g). Despite oscillations, a clear horizontal trend is observed at all the time snapshots for $n_x \geq 80$, in agreement with the conclusions of Section 4.2. Above that threshold, the uniformity index appears to converge to

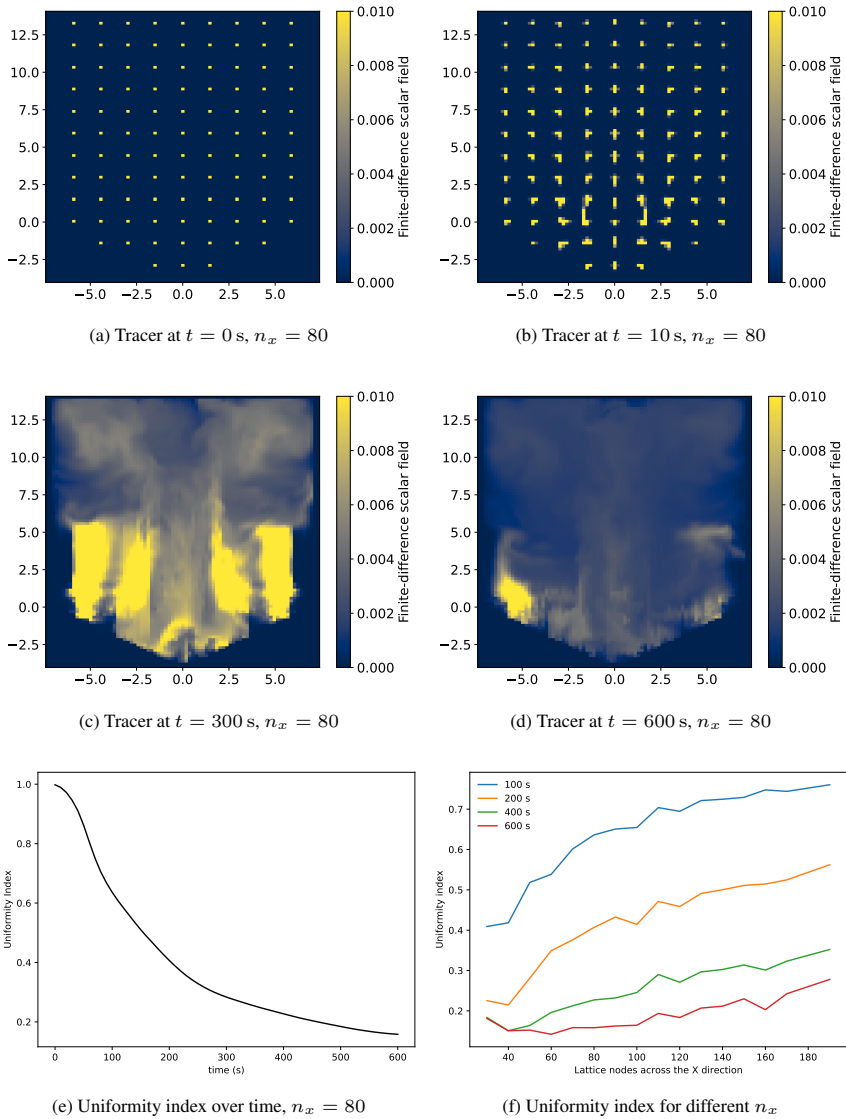
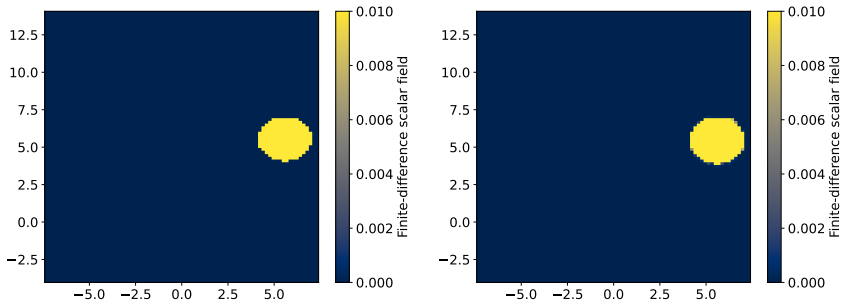
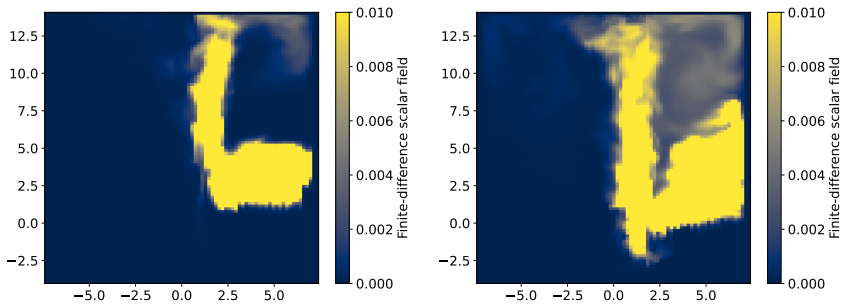
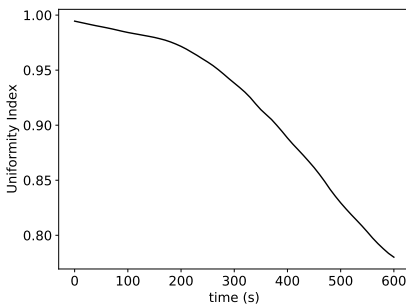
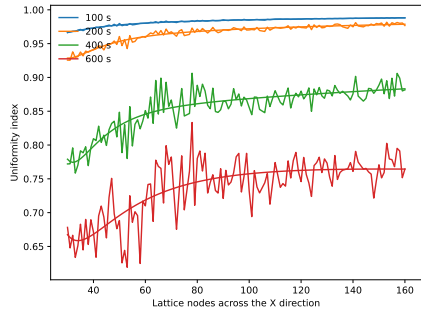
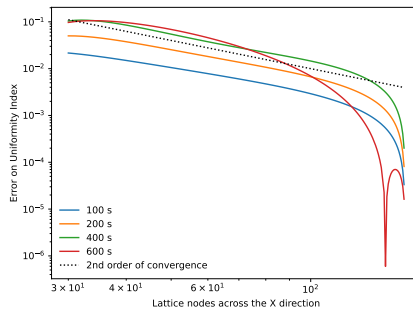


Fig. 7: “Sparse” results, 2.5% TS sludge, 50 mm bubble size.

475 approximately second order, and its relative error falls below 5%. This observation:
 476 (i) indicates that the “Ball” configuration is less affected by numerical diffusivity than
 477 the “Sparse”, and is therefore the most suitable to investigate the model’s behaviour
 478 under variation of its parameters; and (ii) further confirms mesh independence for
 479 $n_x \geq 80$ wherever the initial conditions allow one to ignore numerical diffusivity.

(a) Tracer at $t = 0$ s, $n_x = 80$ (b) Tracer at $t = 10$ s, $n_x = 80$ (c) Tracer at $t = 300$ s, $n_x = 80$ (d) Tracer at $t = 600$ s, $n_x = 80$ (e) Uniformity index over time, $n_x = 80$ (f) Uniformity index for different n_x (g) Relative error on the uniformity index for different n_x **Fig. 8:** “Ball” results, 2.5% TS sludge, 50 mm bubble size.

480 **4.4 Lagrangian subcycles**

481 Figure 9 reports qualitative snapshots, taken at 3600 s, of flow patterns, viscosity
482 and scalar tracer field ϕ , for two different numbers of Lagrangian subcycles (*viz.*, 20
483 and 400). No qualitative difference between the results of the different numbers of
484 Lagrangian timesteps can be identified. Further, in Figure 10, vortex position and the
485 value of the uniformity index at different times are reported as a function of the num-
486 ber of Lagrangian subcycles, for both the “Sparse” and “Ball” initial conditions. A
487 best fit of the form $UI = \sum_i a_i s^{-n}$, $0 \leq i \leq 2$, is reported. Apart from local oscil-
488 lations attributable to noise, the relevant parameters are observed to be independent
489 from the number of Lagrangian subcycles, within a relative error of $\sim 10^{-2}$.

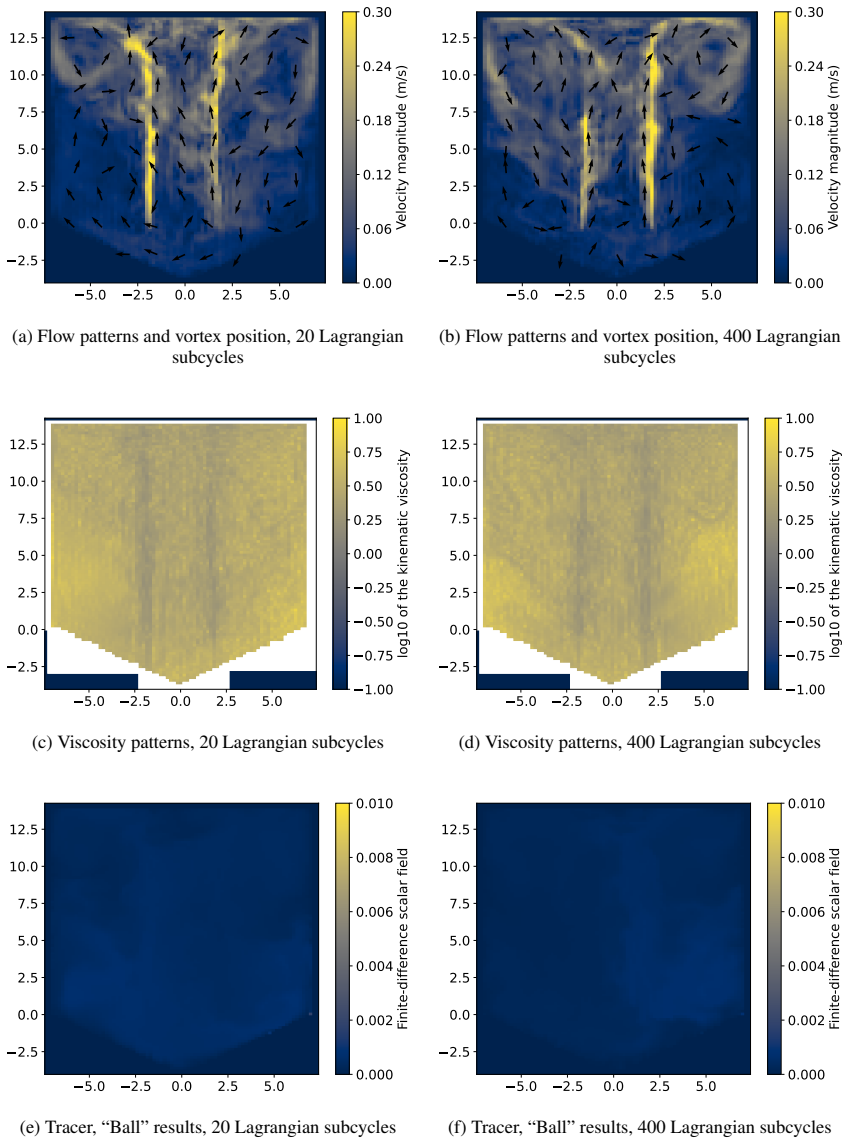


Fig. 9: Flow patterns, vortex position, viscosity patterns and tracer for different numbers of Lagrangian subcycles at $t = 3600$ s. 2.5% TS sludge, $n_x = 80$, 50 mm bubble diameter.

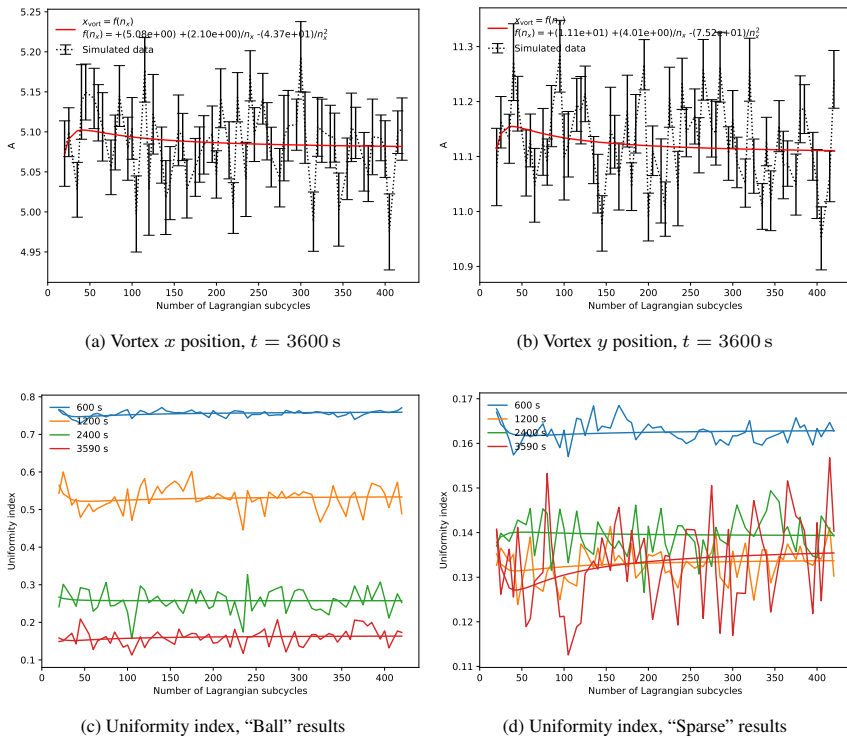


Fig. 10: Dependence on number of Lagrangian subcycles, $n_x = 80$, 2.5% TS sludge, 50 mm bubble size.

4.5 Bubble size

Figure 11 reports qualitative snapshots, taken at 840 s, of flow patterns, viscosity and scalar tracer field ϕ , for two different bubble sizes (*viz.*, 15 and 50 mm). Flow patterns snapshots (Figures 11a and 11b) display qualitatively more intense flow patterns in simulations with smaller bubble size. The latter also present a more prominent presence of small-scale structures, indicating a higher level of turbulence. Conversely, viscosity flow patterns (Figures 11c and 11d) and final tracer ϕ distribution (Figures 11e and 11f) are not found to be affected by the choice of bubble size.

From these observations, it can be argued that smaller bubbles manage to mix the system faster thanks to more intense flow patterns and turbulence intensity, whilst the final level of mixing remains unaffected. This picture is confirmed by the quantitative picture (Figure 12). The vortex positions (Figures 12a and 12b) do not provide relevant information due to the large uncertainty bars. However, the uniformity index (Figure 12c), for early timesteps (140 s) clearly shows that smaller bubble sizes produce lower UI values, with a difference of UI value between 50 mm and 15 mm bubble sizes of 0.083, corresponding to around 18% of 15 mm bubble size's UI value. This difference decreases for further timesteps, with the relative error at the final timestep being below 10^{-2} .

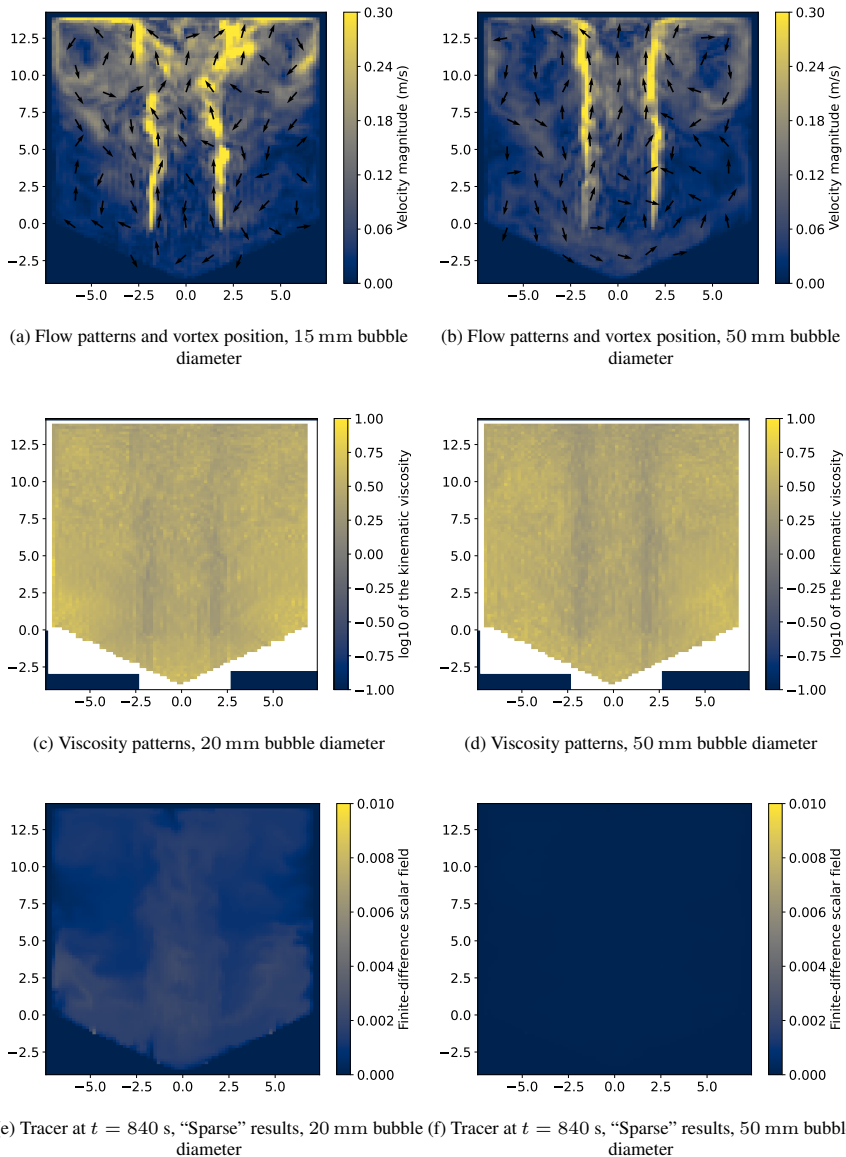
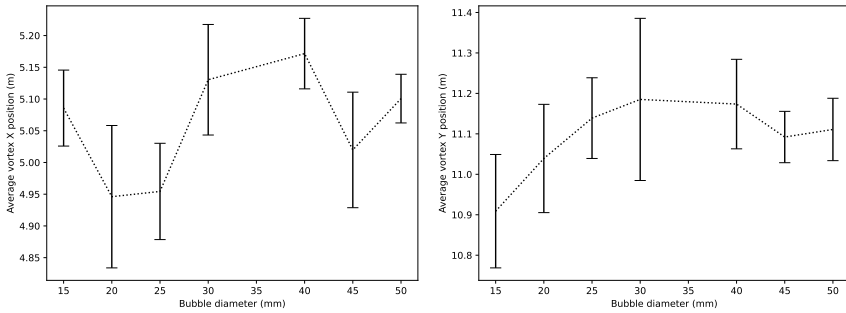
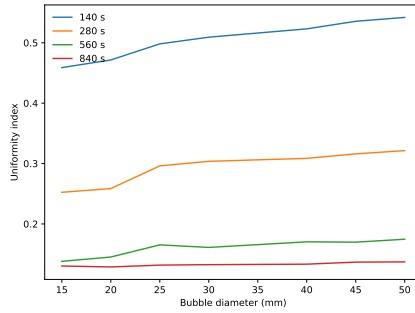


Fig. 11: Flow patterns, vortex position, viscosity patterns and tracer for different bubble sizes at $t = 840$ s. 2.5% TS sludge, $n_x = 80$, 100 Lagrangian subcycles.

(a) Vortex x position, $t = 840$ s(b) Vortex y position, $t = 840$ s

(c) Uniformity index

Fig. 12: Dependence on bubble size. “Sparse” results, $n_x = 80$, 2.5% TS sludge.

4.6 Scaling-up

A strong scaling-up test was performed (Figure 13) on up to 12 Intel Xeon Gold Skylake cores, each containing 40 CPU cores. The simulations were run selecting

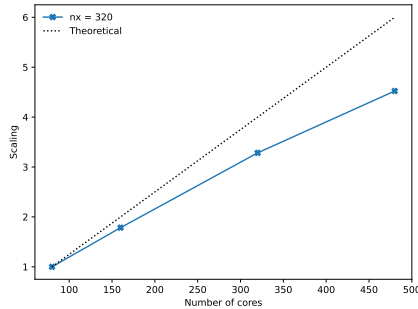


Fig. 13: Strong scaling, 2 to 12 nodes, each with 40 CPUs.

$n_x = 320$ (corresponding to over 32,113,000 cells), 50 mm bubble size, for 60 s simulated time. The scale-up clearly shows an increasing trend throughout the whole range of number of cores, with a loss of efficiency of less than 25% at the highest number of cores. Such loss of efficiency is likely due to the non-scalable inter-core communication taking place at the streaming phase; and to the Lagrangian particles. Indeed, within OpenLB, a Lagrangian particle is simulated by the CPU core responsible for the subdomain where the given particle is located; this means that non-scalable operations occur when a particle crosses a subdomain division as its data are communicated from the target to the destination CPU; and asymmetric load balancing occurs when the particles are not distributed uniformly throughout the computational domain (which is the case for the simulation work described within this article).

5 Discussion

The results reported in Section 4.2 show that the flow patterns are grid independent for $n_x \gtrsim 80$. However, the noise manifesting itself as oscillations in Figure 6 makes the determination of the order of convergence challenging. Similar considerations hold for the uniformity index: once the grid-dependent effect of numerical diffusion is singled out, UI displays grid independence for a similar value of $n_x \gtrsim 80$, with analogue considerations about noise (Figure 8f).

The results reported in Section 4.4 indicate that the simulations are independent of the number of Lagrangian subcycles. As such, the number of Lagrangian subcycles remains a non-physical tuning parameter, to be tuned depending on the particular application and the specific bubble size, to strike the best balance between numerical expense (*i.e.*, the numerical expense is proportional to the number of Lagrangian subcycles), and stability (*i.e.*, the Lagrangian solver becomes unstable if the number of Lagrangian timesteps falls below a threshold dependent on specific application and bubble size).

538 In Section 4.5, bubble size is shown to affect flow the patterns and the transient
539 evolution of the uniformity index, but not the final value of UI — or in other words,
540 the prediction of steady-state mixing quality. This is in agreement with the obser-
541 vations on the same geometry, applying a second-order Finite-Volume Reynolds-
542 Averaged-Navier-Stokes model with Reynolds-stress turbulence model and the same
543 power-law rheology model, on OpenFOAM 2.3.0 (www.openfoam.org/version/2-3-
544 0) [17, 20, 23].

545 Overall, the Lattice-Boltzmann predictions of flow patterns, uniformity index
546 and degree of mixing produced by the numerical work presented here are in
547 agreement with observations from the above-mentioned Finite-Volume CFD work
548 [17, 20, 23]. However, the Lattice-Boltzmann model presented here offers two critical
549 advantages over the previous Finite-Volume, specifically:

550 **(i) Numerical efficiency.** Lattice-Boltzmann runs with $n_x = 80$ need around
551 10,500 CPUs to run over grids of 536,171 cells for 600–3600 s simulated time,
552 for a specific resource usage of $5.4\text{--}33 \cdot 10^{-6}$ CPUs per s per cell. In contrast, the
553 Finite-Volume analogue took around 13,500,000 CPUs for running over a grid of
554 394,400 cells for 300 s simulated time on 36 Intel Xeon E5-2690 v3 Haswell (2.6
555 GHz) cores, for a specific resource usage of 0.11 CPUs per s per cell. This makes
556 the Lattice-Boltzmann model over 1,000 times faster than the Finite-Volume model
557 previously used in the literature to solve this problem. Similarly, the LES simulations
558 performed in [24] for a full-scale mechanically-mixed digester were conducted on
559 188,289 cells for around 60 s simulated time and took 1,205,200 CPUs, for a specific
560 resource usage of 0.11 CPUs per s per cell—the same value as [17, 20, 23]. Although
561 the present Lattice-Boltzmann work and the previous Finite-Volume are conducted
562 on different machines, the large performance difference between this and the previ-
563 ous models, as well as the similarity in performance between [17, 20, 23] and [24],
564 allow us to confidently rule out any detrimental effect attributable to differences in
565 hardware.

566 **(ii) Resolution.** Lattice-Boltzmann’s best balance between numerical efficiency
567 and precision was found to be $n_x = 80$, for 536,171 cells (Section 4.2). By contrast,
568 the same balance returned 98,420 cells for a $\pi/6$ wedge of the computational domain
569 in the Finite-Volume model. This shows that the Lattice-Boltzmann model comfort-
570 ably allows much finer grids than the Finite-Volume, thereby producing much more
571 detailed predictions. In fact, the Lattice-Boltzmann model allowed a level of detail of
572 the flow patterns, especially concerning smaller-scale turbulent patterns (Figures 11a
573 and 11b), which would be unachievable in the Finite-Volume results reported in
574 [17, 23] because of the above-mentioned difference in numerical efficiency and
575 Finite-Volume’s scaling-up problems [22].

576 **(iii) Scaleup.** Scaling-up performance is discussed in Section 4.6. Despite the
577 limiting factors discussed therein, the strong-scaling plot (Figure 13) clearly shows
578 an increasing trend, without reaching a plateau at 480 cores (it was not possible
579 to perform simulations with more cores due to hardware limitations). This consti-
580 tutes a notable improvement over previous Finite-Volume models, as the plateau was
581 previously reached at 36 cores [17, 23].

582 Considering the usage of cache memory. Lattice-Boltzmann methods are
583 memory-intensive: the model presented here uses 32 floats per lattice cell, much
584 more than the previous Finite-Volume (which uses 5 floats per cell). This high mem-
585 ory usage does not usually pose a limitation to numerical performance as access to
586 cache memory is fast—and indeed, it did not pose a limitation to the performance of
587 the runs described here. However, care should be taken in checking that the avail-
588 able cache memory can meet a run’s memory requirement, before performing the run
589 itself. `OpenLB` maps the computational domain into a lattice, or `SuperLattice`
590 object, which is in turn divided into sub-lattices, or `BlockLattice` objects. Each
591 `BlockLattice` is loaded onto the cache memory of a single CPU [51]. As
592 such, increasing the number of cores usually resolves possible problems of short-
593 age of memory. Considering the effectiveness of this strategy in preventing memory
594 over-usage, and considering that memory usage does not constitute a bottleneck to
595 numerical performance, we did not perform a comparison between memory usage of
596 the model presented here, and its Finite-Volume predecessors [17, 23].

597 **6 Conclusions**

598 A Lattice-Boltzmann LES model of a full-scale, biogas-mixed anaerobic digester
599 has been presented for the first time. Scaleup, convergence and the effects of bubble
600 size and number of Lagrangian subcycles on the model predictions concerning the
601 digester’s hydrodynamics have been assessed.

602 A comparison between Lattice-Boltzmann and Finite-Volume on an analogue
603 applications shows that the former is over 1,000 times more computationally effi-
604 cient, allows resolution of flow patterns in much more detail, and allow a feasible,
605 resource-effective usage of LES in anaerobic digestion modelling for the first time.
606 Thus, the work presented here is a comparison between two specific models being
607 used to solve a problem of significant interest and relevance to the wastewater indus-
608 try. It should not be considered as a benchmark in a strict sense—such benchmark
609 work would require tests on a wide range of models being conducted on the same
610 hardware running under the same conditions, and is out of the scope of this research.
611 Notwithstanding this limitation, it can be concluded that the Lattice-Boltzmann is a
612 more convenient modelling choice for full-scale gas mixing in anaerobic digestion,
613 than the most common second-order Finite-Volume approaches.

614 Industries and consultancies will be able to use the results described here as
615 guidance to improve full-scale digesters’ mixing efficiency via UI maximization. In
616 this respect, the code used here will be available in a future official release of the
617 `OpenLB` package.

618 **Acknowledgments**

619 The authors gratefully acknowledge Peter Vale and Severn Trent Ltd. for kindly
620 providing the details of the digester geometry.

621 This research was funded by the UKRI Engineering and Physical Sciences
622 Research Council via EPSRC Grant (EP/R01485X/1, Computational Methods for
623 Anaerobic Digestion Optimization, “CoMANDO”). The authors would like to thank

624 the University of Bradford and University of Liverpool's High Performance Com-
625 puting (HPC) Services, where part of the computational work was carried out (*i.e.*,
626 the scaling-up was performed at the University Liverpool, and the remainder at the
627 University of Bradford). Krause's contribution was made possible by funding from
628 the German Research Foundation (DFG 436212129). No contribution other than
629 financial support came from the above-mentioned funding bodies.

630 References

- 631 [1] WWAP (World Water Assessment Programme): The United Nations World
632 Water Development Report 4: Managing Water under Uncertainty and Risk.
633 Technical report, UNESCO, Paris (2012). ISBN: 978-92-3-104235-5
- 634 [2] European Environment Agency: Waterbase - UWWTD: Urban Waste Water
635 Treatment Directive – reported data. Technical report (2015)
- 636 [3] Eurostat: Sewage sludge production and disposal (2021). [http://appsso.eurostat.
637 ec.europa.eu/nui/show.do?lang=en&dataset=env_ww_spd](http://appsso.eurostat.ec.europa.eu/nui/show.do?lang=en&dataset=env_ww_spd) Accessed 2021-02-
638 08
- 639 [4] Owen, W.F.: Anaerobic Treatment Processes. In: Energy in Wastewater Treat-
640 ment. Prentice-Hall, Inc., Englewood Cliffs, NJ (1982)
- 641 [5] Kress, P., Nägele, H.J., Oechsner, H., Ruile, S.: Effect of agitation time on nutri-
642 ent distribution in full-scale CSTR biogas digesters. *Bioresource Technology*
643 **247**(September 2017), 1–6 (2018). [https://doi.org/10.1016/j.biortech.2017.09.
644 054](https://doi.org/10.1016/j.biortech.2017.09.054). Publisher: Elsevier
- 645 [6] Vesvikar, M.S., Al-Dahhan, M.H.: Flow pattern visualization in a mimic anaer-
646 obic digester using CFD. *Biotechnology and Bioengineering* **89**(6), 719–732
647 (2005). <https://doi.org/10.1002/bit.20388>
- 648 [7] Karim, K., Thoma, G.J., Al-Dahhan, M.H.: Gas-lift digester configuration
649 effects on mixing effectiveness. *Water Research* **41**(14), 3051–3060 (2007).
650 <https://doi.org/10.1016/j.watres.2007.03.042>
- 651 [8] Meroney, R.N., Colorado, P.E.: CFD simulation of mechanical draft tube mix-
652 ing in anaerobic digester tanks. *Water Research* **43**(4), 1040–1050 (2009).
653 <https://doi.org/10.1016/j.watres.2008.11.035>
- 654 [9] Terashima, M., Goel, R., Komatsu, K., Yasui, H., Takahashi, H., Li, Y.Y., Noike,
655 T.: CFD simulation of mixing in anaerobic digesters. *Bioresource Technol-
656 ogy* **100**(7), 2228–2233 (2009). <https://doi.org/10.1016/j.biortech.2008.07.069>.
657 Publisher: Elsevier Ltd ISBN: 0960-8524
- 658 [10] Wu, B.: CFD simulation of gas and non-Newtonian fluid two-phase flow in
659 anaerobic digesters. *Water Research* **44**(13), 3861–3874 (2010). <https://doi.org/>

660 [10.1016/j.watres.2010.04.043](https://doi.org/10.1016/j.watres.2010.04.043). Publisher: Elsevier Ltd

661 [11] Bridgeman, J.: Computational fluid dynamics modelling of sewage sludge mixing in an anaerobic digester. *Advances in Engineering Software* **44**(1), 54–62
662 (2012). <https://doi.org/10.1016/j.advengsoft.2011.05.037>

664 [12] Sindall, R.C., Bridgeman, J., Carliell-Marquet, C.: Velocity gradient
665 as a tool to characterise the link between mixing and biogas production in anaerobic waste digesters. *Water Science and Technology*
666 **67**(12), 2800–2806 (2013). <https://doi.org/10.2166/wst.2013.206>. ISBN:
667 <http://www.iwaponline.com/wst/06712/wst067122800.htm>
668

669 [13] Craig, K.J., Nieuwoudt, M.N., Niemand, L.J.: CFD simulation of anaerobic
670 digester with variable sewage sludge rheology. *Water Research* **47**(13), 4485–
671 4497 (2013). <https://doi.org/10.1016/j.watres.2013.05.011>. Publisher: Elsevier
672 Ltd ISBN: 1879-2448 (Electronic) 0043-1354 (Linking)

673 [14] Dapelo, D., Alberini, F., Bridgeman, J.: Euler-Lagrange CFD modelling of
674 unconfined gas mixing in anaerobic digestion. *Water Research* **85**, 497–511
675 (2015). <https://doi.org/10.1016/j.watres.2015.08.042>

676 [15] Hurtado, F.J., Kaiser, A.S., Zamora, B.: Fluid dynamic analysis of a contin-
677 uous stirred tank reactor for technical optimization of wastewater digestion.
678 *Water Research* **71**, 282–293 (2015). [https://doi.org/10.1016/j.watres.2014.11.](https://doi.org/10.1016/j.watres.2014.11.053)
679 [053](https://doi.org/10.1016/j.watres.2014.11.053). Publisher: Elsevier Ltd

680 [16] Zhang, Y., Yu, G., Yu, L., Siddhu, M.A.H., Gao, M., Abdeltawab, A.A., Al-
681 Deyab, S.S., Chen, X.: Computational fluid dynamics study on mixing mode
682 and power consumption in anaerobic mono- and co-digestion. *Bioresource*
683 *Technology* **203**, 166–172 (2016). [https://doi.org/10.1016/j.biortech.2015.12.](https://doi.org/10.1016/j.biortech.2015.12.023)
684 [023](https://doi.org/10.1016/j.biortech.2015.12.023)

685 [17] Dapelo, D., Bridgeman, J.: Euler-Lagrange Computational Fluid Dynamics
686 simulation of a full-scale unconfined anaerobic digester for wastewater sludge
687 treatment. *Advances in Engineering Software* **117**, 153–169 (2018). [https://doi.](https://doi.org/10.1016/j.advengsoft.2017.08.009)
688 [org/10.1016/j.advengsoft.2017.08.009](https://doi.org/10.1016/j.advengsoft.2017.08.009). Publisher: Elsevier Ltd

689 [18] Lebranchu, A., Delaunay, S., Marchal, P., Blanchard, F., Pacaud, S., Fick, M.,
690 Olmos, E.: Impact of shear stress and impeller design on the production of
691 biogas in anaerobic digesters. *Bioresource Technology* **245**(June), 1139–1147
692 (2017). <https://doi.org/10.1016/j.biortech.2017.07.113>. Publisher: Elsevier

693 [19] Meister, M., Rezavand, M., Ebner, C., Pümpel, T., Rauch, W.: Mixing non-
694 Newtonian flows in anaerobic digesters by impellers and pumped recirculation.
695 *Advances in Engineering Software* **115**(February 2017), 194–203 (2018). <https://doi.org/10.1016/j.advengsoft.2017.09.015>. Publisher: Elsevier
696

- 697 [20] Dapelo, D., Bridgeman, J.: A CFD strategy to retrofit an anaerobic digester
698 to improve mixing performance in wastewater treatment. *Water Science and*
699 *Technology* **81**(8), 1646–1657 (2020). <https://doi.org/10.2166/wst.2020.086>
- 700 [21] Tsoutsanis, P., Antoniadis, A.F., Jenkins, K.W.: Improvement of the compu-
701 tational performance of a parallel unstructured WENO finite volume CFD
702 code for Implicit Large Eddy Simulation. *Computers and Fluids* **173**, 157–
703 170 (2018). <https://doi.org/10.1016/j.compfluid.2018.03.012>. Publisher: Else-
704 vier Ltd
- 705 [22] Hawkes, J., Vaz, G., Phillips, A.B., Cox, S.J., Turnock, S.R.: On the strong
706 scalability of maritime CFD. *Journal of Marine Science and Technology* **23**(1),
707 81–93 (2018). <https://doi.org/10.1007/s00773-017-0457-7>. Publisher: Springer
708 Japan
- 709 [23] Dapelo, D., Bridgeman, J.: Assessment of mixing quality in full-scale, biogas-
710 mixed anaerobic digestion using CFD. *Bioresource Technology* **265**, 480–489
711 (2018). <https://doi.org/10.1016/j.biortech.2018.06.036>. Publisher: Elsevier
- 712 [24] Wu, B.: Large eddy simulation of mechanical mixing in anaerobic digesters.
713 *Biotechnology and Bioengineering* **109**(3), 804–812 (2012). [https://doi.org/10.](https://doi.org/10.1002/bit.24345)
714 [1002/bit.24345](https://doi.org/10.1002/bit.24345)
- 715 [25] Abas, A., Abdullah, M., Ishak, M., As, N., Khor, S.F.: Lattice Boltzmann and
716 Finite Volume simulations of multiphase flow in BGA encapsulation process
717 **10**(17) (2015)
- 718 [26] Gaedtke, M., Wachter, S., Rädle, M., Nirschl, H., Krause, M.J.: Application of
719 a lattice Boltzmann method combined with a Smagorinsky turbulence model to
720 spatially resolved heat flux inside a refrigerated vehicle. *Computers & Mathe-*
721 *matics with Applications* **76**(10), 2315–2329 (2018). [https://doi.org/10.1016/j.](https://doi.org/10.1016/j.camwa.2018.08.018)
722 [camwa.2018.08.018](https://doi.org/10.1016/j.camwa.2018.08.018). Accessed 2023-03-05
- 723 [27] Haussmann, M., Ries, F., Jeppener-Haltenhoff, J.B., Li, Y., Schmidt, M., Welch,
724 C., Illmann, L., Böhm, B., Nirschl, H., Krause, M.J., Sadiki, A.: Evaluation of
725 a Near-Wall-Modeled Large Eddy Lattice Boltzmann Method for the Analysis
726 of Complex Flows Relevant to IC Engines. *Computation* **8**(2), 43 (2020). [https:](https://doi.org/10.3390/computation8020043)
727 [//doi.org/10.3390/computation8020043](https://doi.org/10.3390/computation8020043)
- 728 [28] Reinke, F., Hafen, N., Haussmann, M., Novosel, M., Krause, M.J., Dittler,
729 A.: Applied Geometry Optimization of an Innovative 3D-Printed Wet-Scrubber
730 Nozzle with a Lattice Boltzmann Method. *Chemie Ingenieur Technik* **94**(3),
731 348–355 (2022). <https://doi.org/10.1002/cite.202100151>. Accessed 2023-03-
732 05
- 733 [29] Succi, S.: Lattice Boltzmann 2038. *Europhysics Letters* **109**(5), 50001 (2015).
734 <https://doi.org/10.1209/0295-5075/109/50001>. ISBN: 0295-5075

- 735 [30] Trunk, R., Henn, T., Dörfler, W., Nirschl, H., Krause, M.J.: Inertial dilute par-
736 ticulate fluid flow simulations with an Euler–Euler lattice Boltzmann method.
737 *Journal of Computational Science* **17**, 438–445 (2016). [https://doi.org/10.1016/](https://doi.org/10.1016/j.jocs.2016.03.013)
738 [j.jocs.2016.03.013](https://doi.org/10.1016/j.jocs.2016.03.013). Publisher: Elsevier B.V.
- 739 [31] Maier, M.L., Henn, T., Thaeter, G., Nirschl, H., Krause, M.J.: Multiscale Sim-
740 ulation with a Two-Way Coupled Lattice Boltzmann Method and Discrete
741 Element Method. *Chemical Engineering and Technology* **40**(9), 1591–1598
742 (2017). <https://doi.org/10.1002/ceat.201600547>
- 743 [32] Krause, M.J., Klemens, F., Henn, T., Trunk, R., Nirschl, H.: Particle flow
744 simulations with homogenised lattice Boltzmann methods. *Particuology* **34**,
745 1–13 (2017). <https://doi.org/10.1016/j.partic.2016.11.001>. Publisher: Chinese
746 Society of Particuology
- 747 [33] Rettinger, C., Rude, U.: A comparative study of fluid-particle coupling meth-
748 ods for fully resolved lattice Boltzmann simulations. *Computers and Flu-*
749 *ids* **154**, 74–89 (2017). <https://doi.org/10.1016/j.compfluid.2017.05.033>. arXiv:
750 1702.04910 Publisher: Elsevier Ltd ISBN: 0045-7930
- 751 [34] Dapelo, D., Trunk, R., Krause, M.J., Bridgeman, J.: Towards Lattice-Boltzmann
752 modelling of unconfined gas mixing in anaerobic digestion. *Computers and*
753 *Fluids* **180**, 11–21 (2019). <https://doi.org/10.1016/j.compfluid.2018.12.008>.
754 Publisher: Elsevier Ltd
- 755 [35] Dapelo, D., Trunk, R., Krause, M.J., Cassidy, N., Bridgeman, J.: The appli-
756 cation of Buckingham pi theorem to Lattice-Boltzmann modelling of sewage
757 sludge digestion. *Computers and Fluids* **209**, 104632 (2020). [https://doi.org/10.](https://doi.org/10.1016/j.compfluid.2020.104632)
758 [1016/j.compfluid.2020.104632](https://doi.org/10.1016/j.compfluid.2020.104632). Publisher: Elsevier Ltd
- 759 [36] Wu, B.: CFD simulation of mixing in egg-shaped anaerobic digesters. *Water*
760 *Research* **44**(5), 1507–1519 (2010). [https://doi.org/10.1016/j.watres.2009.10.](https://doi.org/10.1016/j.watres.2009.10.040)
761 [040](https://doi.org/10.1016/j.watres.2009.10.040). Publisher: Elsevier Ltd
- 762 [37] Sindall, R.C., Dapelo, D., Leadbeater, T., Bridgeman, J.: Positron emission
763 particle tracking (PEPT): A novel approach to flow visualisation in lab-
764 scale anaerobic digesters. *Flow Measurement and Instrumentation* **54**, 250–264
765 (2017). <https://doi.org/10.1016/j.flowmeasinst.2017.02.009>
- 766 [38] Zhang, M., Zhang, L., Jiang, B., Yin, Y., Li, X.: Calculation of Metzner Con-
767 stant for Double Helical Ribbon Impeller by Computational Fluid Dynamic
768 Method. *Chinese Journal of Chemical Engineering* **16**(5), 686–692 (2008).
769 [https://doi.org/10.1016/S1004-9541\(08\)60141-X](https://doi.org/10.1016/S1004-9541(08)60141-X). Publisher: Chemical Indus-
770 try and Engineering Society of China (CIESC) and Chemical Industry Press
771 (CIP)
- 772 [39] Wu, B., Chen, S.: CFD simulation of non-Newtonian fluid flow in anaerobic

- 773 digesters. *Biotechnology and Bioengineering* **99**(3), 700–711 (2008). <https://doi.org/10.1002/bit.21613>
774
- 775 [40] Landry, H., Laguë, C., Roberge, M.: Physical and rheological properties of
776 manure products. *Applied Engineering in Agriculture* **20**(3), 277–288 (2004).
777 <https://doi.org/10.13031/2013.16061>. ISBN: 0883-8542
- 778 [41] van Wachem, B.G.M., Almstedt, A.E.: Methods for multiphase computational
779 fluid dynamics. *Chemical Engineering Journal* **96**(1-3), 81–98 (2003). <https://doi.org/10.1016/j.cej.2003.08.025>. ISBN: 1385-8947
780
- 781 [42] Verlet, L.: Computer Experiments on Classical Fluids. I. Thermodynamical
782 Properties of Lennard-Jones Molecules. *Physical Review* **159**(1), 98–103
783 (1967). <https://doi.org/10.1103/PhysRev.159.98>
- 784 [43] Morsi, S.A., Alexander, A.J.: An investigation of particle trajectories in two-
785 phase flow systems. *Journal of Fluid Mechanics* **55**(02), 193–208 (1972). <https://doi.org/10.1017/S0022112072001806>
786
- 787 [44] Kruger, T., Kasumaatmaja, H., Kuzmim, A., Shardt, O., Silva, G., Vigen, E.M.:
788 The Lattice Boltzmann Method. Springer, ??? (2017). <https://doi.org/10.1007/978-3-319-44649-3>. arXiv: 1011.1669v3 Issue: March 2015 ISSN: 1098-6596
789
- 790 [45] Bhatnagar, P.L., Gross, E.P., Krook, M.: A model for collision processes in
791 gases. I. Small amplitude processes in charged and neutral one-component
792 systems. *Physical Review* **94**(3), 511–525 (1954). <https://doi.org/10.1103/PhysRev.94.511>. ISBN: 0031-899X
793
- 794 [46] Boyd, J., Buick, J., Green, S.: A second-order accurate lattice Boltzmann
795 non-Newtonian flow model. *Journal of Physics A: Mathematical and General* **39**(46), 14241–14247 (2006). <https://doi.org/10.1088/0305-4470/39/46/001>. ISBN: 0305-4470\n1361-6447
796
797
- 798 [47] Hou, S., Sterling, J., Chen, S., Doolen, G.D.: A Lattice Boltzmann Subgrid
799 Model for High Reynolds Number Flows. In: Lawniczak, A.T., Kapral, R. (eds.) *Pattern Formation and Lattice Gas Automata* vol. 6. AMS -
800 Fields Institute Communications, ??? (1996). arXiv: comp-gas/9401004.
801 http://books.google.com/books?hl=en&lr=&id=TI dy6-ItW7YC&oi=fnd&pg=PA151&dq=A+Lattice+Boltzmann+Subgrid+Model+for+High+Reynolds+Number+Flows&ots=zqrEqXjMNL&sig=_76MYxU-XPd2n1iKsPD5rIJQ7-Q
802
803
804
805
- 806 [48] Guo, Z., Zheng, C., Shi, B.: Discrete lattice effects on the forcing term in the
807 lattice Boltzmann method. *Physical Review E - Statistical Physics, Plasmas, Fluids, and Related Interdisciplinary Topics* (2002). <https://doi.org/10.1103/PhysRevE.65.046308>
808
809

- 810 [49] Falcucci, G., Amati, G., Fanelli, P., Krastev, V.K., Polverino, G., Por-
811 firi, M., Succi, S.: Extreme flow simulations reveal skeletal adaptations of
812 deep-sea sponges. *Nature* **595**(7868), 537–541 (2021). [https://doi.org/10.1038/
813 s41586-021-03658-1](https://doi.org/10.1038/s41586-021-03658-1). Accessed 2023-05-09
- 814 [50] Succi, S., Amati, G., Bernaschi, M., Falcucci, G., Lauricella, M., Montes-
815 sori, A.: Towards Exascale Lattice Boltzmann computing. *Computers &
816 Fluids* **181**, 107–115 (2019). <https://doi.org/10.1016/j.compfluid.2019.01.005>.
817 Accessed 2023-05-09
- 818 [51] Krause, M.J., Kummerlaender, A., Avis, S.J., Kusumaatmaja, H., Dapelo,
819 D., Klemens, F., Gaedtke, M., Hafen, N., Mink, A., Trunk, R., Marquardt,
820 J.E., Maier, M.-L., Haussmann, M., Simonis, S.: OpenLB-Open source lattice
821 Boltzmann code. *Computers and Mathematics with Applications* **81**, 258–288
822 (2021). <https://doi.org/10.1016/j.camwa.2020.04.033>. Publisher: Elsevier Ltd
- 823 [52] Trunk, R., Bretl, C., Thäter, G., Nirschl, H., Dorn, M., Krause, M.J.: A Study on
824 Shape-Dependent Settling of Single Particles with Equal Volume Using Surface
825 Resolved Simulations. *Computation* **9**(4), 40 (2021). [https://doi.org/10.3390/
826 computation9040040](https://doi.org/10.3390/computation9040040). Accessed 2023-05-10
- 827 [53] Siodlaczek, M., Gaedtke, M., Simonis, S., Schweiker, M., Homma, N., Krause,
828 M.J.: Numerical evaluation of thermal comfort using a large eddy lattice Boltz-
829 mann method. *Building and Environment* **192**, 107618 (2021). [https://doi.org/
830 10.1016/j.buildenv.2021.107618](https://doi.org/10.1016/j.buildenv.2021.107618). Accessed 2023-05-10
- 831 [54] Mink, A., Schediwy, K., Posten, C., Nirschl, H., Simonis, S., Krause, M.J.:
832 Comprehensive Computational Model for Coupled Fluid Flow, Mass Transfer,
833 and Light Supply in Tubular Photobioreactors Equipped with Glass Sponges.
834 *Energies* **15**(20), 7671 (2022). <https://doi.org/10.3390/en15207671>. Accessed
835 2023-05-10
- 836 [55] Gaedtke, M., Abishek, S., Mead-Hunter, R., King, A., Mullins, B.J., Nirschl,
837 H., Krause, M.J.: Total enthalpy-based lattice Boltzmann simulations of melting
838 in paraffin/metal foam composite phase change materials. *International Journal
839 of Heat and Mass Transfer* **155**, 119870 (2020). [https://doi.org/10.1016/j.
840 ijheatmasstransfer.2020.119870](https://doi.org/10.1016/j.ijheatmasstransfer.2020.119870). Accessed 2023-05-10
- 841 [56] Kummerländer, A., Avis, S., Kusumaatmaja, H., Bukreev., F., Dapelo, D.,
842 Großmann, S., Hafen, N., Holeska, C., Husfeldt, A., Jeßberger, J., Kronberg,
843 L., Marquardt, J.E., Mödl, J., Nguyen, J., Pertzel, T., Simonis, S., Spring-
844 mann, L., Suntoyo, N., Teutscher, D., Zhong, M., Krause, M.J.: OpenLB
845 Release 1.5: Open Source Lattice Boltzmann Code. Zenodo. Language: en
846 (2022). <https://doi.org/10.5281/ZENODO.6469606>. [https://zenodo.org/record/
847 6469606](https://zenodo.org/record/6469606) Accessed 2023-05-10
- 848 [57] Kummerländer, A., Dorn, M., Frank, M., Krause, M.J.: Implicit propagation of

- 849 directly addressed grids in lattice Boltzmann methods. *Concurrency and Com-*
850 *putation: Practice and Experience* **35**(8) (2023). [https://doi.org/10.1002/cpe.](https://doi.org/10.1002/cpe.7509)
851 [7509](https://doi.org/10.1002/cpe.7509). Accessed 2023-05-10
- 852 [58] Kummerlaender, A., Bukreev, F., Berg, S., Dorn, M., Krause, M.J.: Advances
853 in Computational Process Engineering using Lattice Boltzmann Methods on
854 High Performance Computers for Solving Fluid Flow Problems. In: *High Per-*
855 *formance Computing in Science and Engineering '22*. Springer, Solan (CZ)
856 (2022)
- 857 [59] Krause, M.J., Avis, S., Dapelo, D., Hafen, N., Haußmann, M., Gaedtke, M., Kle-
858 mens, F., Kummerländer, A., Maier, M.-L., Mink, A., Ross-Jones, J., Simonis,
859 S., Trunk, R.: OpenLB Release 1.3: Open Source Lattice Boltzmann Code. Zen-
860 do (2019). [https://doi.org/10.5281/](https://doi.org/10.5281/zenodo.3625967)
861 [zenodo.3625967](https://doi.org/10.5281/zenodo.3625967)
- 862 [60] Heuveline, V., Krause, M.J., Latt, J.: Towards a hybrid parallelization of
863 lattice Boltzmann methods. *Computers and Mathematics with Applications*
864 **58**(5), 1071–1080 (2009). <https://doi.org/10.1016/j.camwa.2009.04.001>. Pub-
865 lisher: Elsevier Ltd
- 866 [61] Mohrhard, M., Thäter, G., Bludau, J., Horvat, B., Krause, M.J.: An auto-
867 vecotorization friendly parallel lattice Boltzmann streaming scheme for direct
868 addressing. *Computers and Fluids* **181**, 1–7 (2019). [https://doi.org/10.1016/j.](https://doi.org/10.1016/j.compfluid.2019.01.001)
869 [compfluid.2019.01.001](https://doi.org/10.1016/j.compfluid.2019.01.001). Publisher: Elsevier Ltd
- 870 [62] Dapelo, D., Simonis, S., Krause, M.J., Bridgeman, J.: Lattice–Boltzmann cou-
871 pled models for advection-diffusion flow on a wide range of Péclet numbers.
872 *Journal of Computational Science* **51**(April), 101363 (2021). [https://doi.org/10.](https://doi.org/10.1016/j.jocs.2021.101363)
873 [1016/j.jocs.2021.101363](https://doi.org/10.1016/j.jocs.2021.101363). Publisher: Elsevier B.V.